Constrained Optimization-Based Adaptive Diffraction Pattern Decomposition-Agglomerative Clustering Method for Grain Boundary Detection

LIU, XIAOGE
九州大学大学院総合理工学府総合理工学専攻材料理工学メジャー

Master Thesis

Constrained Optimization-Based Adaptive Diffraction Pattern Decomposition–Agglomerative Clustering Method for Grain Boundary Detection

Science and Engineering of Materials and Devices Major,

Department of Interdisciplinary Engineering Sciences,

Interdisciplinary Graduate School of Engineering Sciences,

Kyushu University

Liu Xiaoge

Supervisor Assoc. Prof. Hikaru SAITO

Date 25th, July 2025

Contents

Chapter 1 Introduction

1.1 Background

Grain boundaries are the interfaces between adjacent crystallites in polycrystalline materials, and their three-dimensional morphology exerts a profound influence on macroscopic material properties. For example, the connectivity of a grain-boundary network governs phenomena such as intergranular crack propagation and boundary-mediated corrosion; only by fully accounting for the three-dimensional arrangement of internal grain boundaries can one accurately predict material performance. Conventionally, grain-boundary studies rely on two-dimensional sectioning techniques (e.g., metallographic imaging or electron backscatter diffraction, EBSD), which often fail to capture boundary continuity and connectivity through the thickness direction. In addition, it should be noted that three-dimensional crystal orientation analysis methods also exist, such as approaches that combine serial sectioning by focused ion beam scanning electron microscopy (FIB-SEM) with EBSD, enabling 3D orientation reconstruction, although these methods involve destructive sectioning and are not the focus of this study. In many engineering materials, achieving a three-dimensional characterization of grain-boundary topography is essential for understanding mechanical, electrical, and chemical behavior [1].

Transmission electron microscopy (TEM), with its high spatial resolution, has become a widespread tool for nanoscale structural investigations [2]. The fundamental strategy for obtaining grain-boundary information via TEM is to raster a finely focused electron beam (on the order of nanometers) across the specimen, record the electron diffraction pattern (“diffraction signature”) at each point, and then determine the local crystal orientation from each pattern to construct orientation or phase maps. This technique—known as orientation mapping—is analogous to SEM-based EBSD but can achieve spatial resolution down to a few nanometers [3].

Building on this basic principle, recent advances in four-dimensional scanning transmission electron microscopy (4D-STEM) have further expanded the use of TEM diffraction for grain-boundary analysis. In 4D-STEM, a converged STEM probe is scanned in a two-dimensional grid while recording the diffraction pattern at each scan position, yielding a “four-dimensional”

dataset that comprises two real-space coordinates and two diffraction dimensions. Analysis of 4D-STEM datasets enables virtual bright-field and dark-field imaging, strain mapping, and direct orientation mapping. In particular, scanning precession electron diffraction (4D-SPED) employs precession of the electron beam to average dynamical diffraction effects, producing more robust and interpretable diffraction signatures. Within a single grain, diffraction patterns remain essentially invariant, whereas across a grain boundary, patterns from adjacent domains exhibit marked differences. By comparing diffraction signatures at neighboring positions, one can thus detect boundaries and reconstruct their morphology [4].

On the basis of the same four-dimensional data structure used in 4D-STEM—two-dimensional real-space grids coupled with two-dimensional diffraction information—dedicated systems such as NanoMEGAS's ASTAR (Automatic Crystal Orientation and phase mapping hardware/software package for TEM) have been developed. ASTAR extends the 4D-STEM concept by incorporating specialized functions such as template matching and automated comparison with precomputed diffraction libraries, enabling direct determination of crystallographic orientation and phase. Fig. 1.1 shows the overall procedure of ASTAR, including beam scanning, signal acquisition through the camera and frame grabber, and subsequent processing to generate phase and orientation maps. Using ASTAR, one can generate orientation and phase maps comparable to those from EBSD, from which high-angle grain boundaries (>15° misorientation) are inferred. Fig. 1.2 shows an example ASTAR orientation map, where high-angle grain boundaries are highlighted in black. Compared with bright-field TEM images, ASTAR orientation mapping provides a more accurate delineation of the grain-boundary network [5].

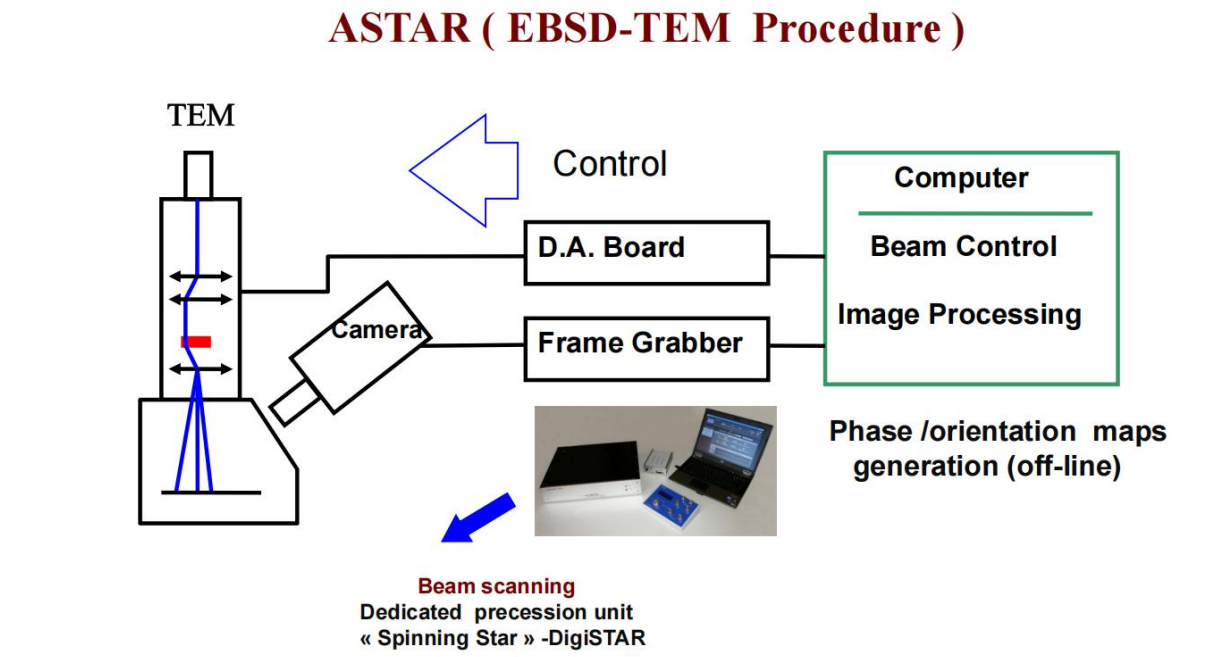

Fig. 1.1 Schematic workflow of the ASTAR system.

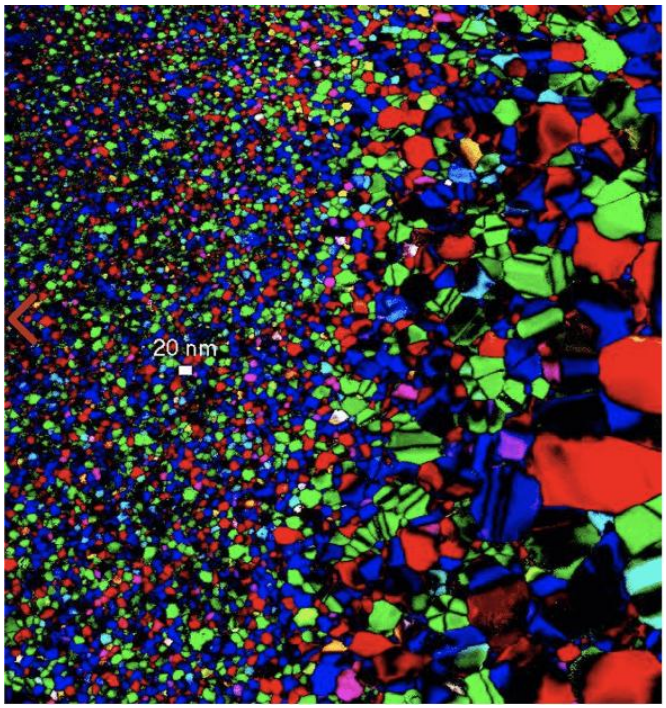

Fig. 1.2 Example of an ASTAR orientation map.

To bridge the discussion from the measurement principles above to the challenges that follow, it is first necessary to clarify the specific type of boundary detection targeted in this study. When a linear electron beam is used in diffraction scanning, the recorded signal represents an integration of all diffraction events occurring along the beam path, meaning that the resulting projection image inevitably contains overlapping contributions from different depths. In conventional approaches such as ASTAR, these overlapping contributions lead to blurred or staircase-like grain boundary representations, which cannot be used directly for accurate reconstruction.

In contrast, the method developed in this study extracts grain boundaries through diffraction-pattern clustering, eliminating depth-mixing artifacts and producing an accurate two-dimensional projection of each grain boundary. Such an accurate 2D projection is the fundamental prerequisite for any valid three-dimensional reconstruction: without it, collecting data from multiple tilt angles would still fail to reproduce the true boundary morphology. Fig. 1.3 illustrates this concept by showing a schematic of grain boundaries output by a Conventional method (e.g., ASTAR), which does not provide sufficiently accurate two-dimensional projections for 3D grain-boundary reconstruction. Accurate projections are a prerequisite for multi-angle data fusion, and methods like ASTAR inherently suffer from misindexing near boundaries, making such reconstruction infeasible.

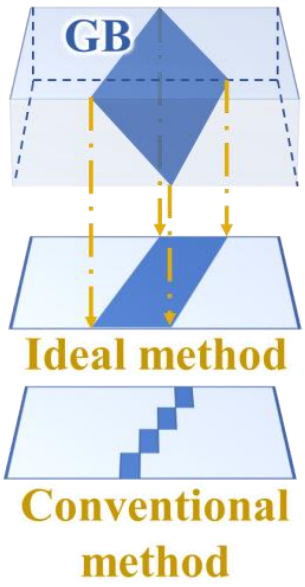

Fig. 1.3 Grain-boundary projection images and a schematic of grain boundaries output by the ASTAR method.

In this context, Sato's master's thesis demonstrated a pioneering attempt by integrating ASTAR orientation mapping with a Multivariate Least Squares (MLS) approach to enhance projection accuracy and to derive partial 3D visualization of grain boundaries [6]. Fig. 1.4 in Sato's abstract illustrates the MLS-based segmentation and the subsequent three-line fitting used to identify boundary edges, showing how boundary regions appear as gradual transitions with contributions from adjacent grains. The MLS approach operates by treating diffraction patterns from neighboring grains as basis patterns and solving for non-negative weight coefficients for each pixel, thereby separating grain interiors from mixed boundary regions. His results confirmed the feasibility of using diffraction-based projections for 3D analysis, while also revealing unresolved challenges—such as limited projection precision in complex microstructures and difficulty in fully isolating boundary signals when pattern matching is incomplete. These issues are further discussed later in this thesis and directly motivate the research direction pursued here.

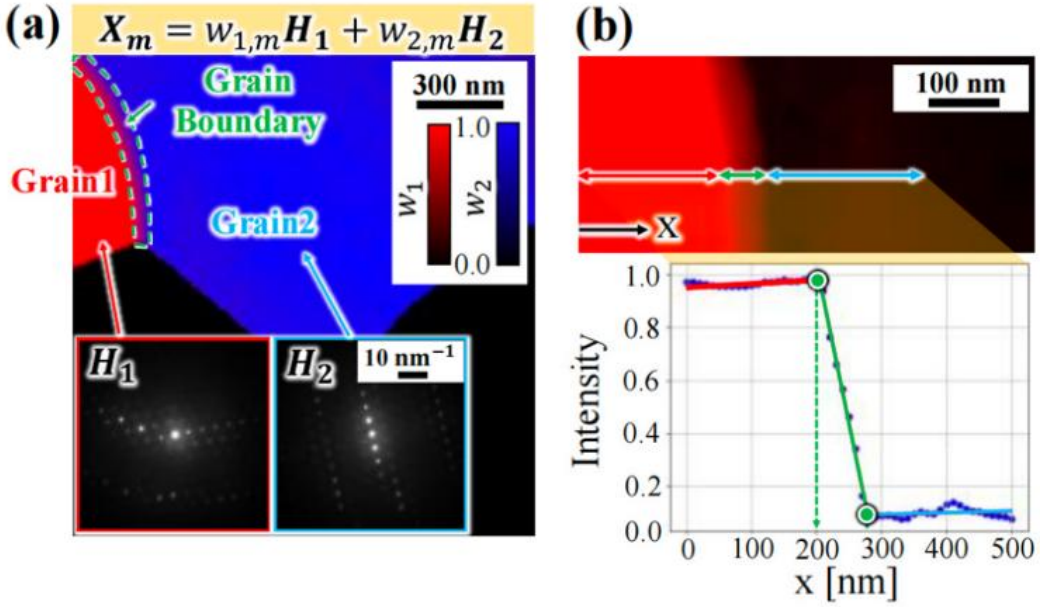

Fig. 1.4 (a) MLS results and (b) three-line fitting applied to the MLS results.

In summary, high-resolution TEM diffraction scanning offers the potential to map grain-boundary distributions at the nanoscale, providing a powerful tool for elucidating the impact of three-dimensional boundary architectures on material properties. Importantly, there have already been successful demonstrations of three-dimensional observation of grain boundaries using TEM techniques. In particular, Sato's work combined ASTAR orientation mapping with the MLS

approach to reconstruct three-dimensional grain-boundary networks, providing valuable proof-of-concept results. These pioneering studies show that 3D grain-boundary visualization with TEM is feasible. Nevertheless, current techniques and methodologies for grain-boundary detection still face significant limitations, motivating further development, as will be discussed in the following “Current Challenges.”

1.2 Current Challenges

1.2.1 Limitations of Template-Matching Methods

Template-matching is among the most widely used techniques for crystallographic orientation analysis in TEM orientation-mapping (e.g., ASTAR). However, it exhibits notable shortcomings, particularly in accurately resolving grain-boundary regions. First, its reliability hinges on a precomputed library of diffraction templates whose fidelity directly affects indexing accuracy. When the specimen contains lattice distortions, defects, or complex texture, the template library cannot faithfully represent the true diffraction patterns, leading to matching errors [7]. For instance, even slight lattice aberrations or dislocation structures have been shown to degrade matching precision significantly [8].

Second, template-matching is computationally intensive and time-consuming. Performing point-by-point matching at every scan position becomes prohibitively expensive as both the scan area and template library size grow, rendering real-time analysis infeasible. In the processing of complex 4D-STEM datasets, template-matching can consume over 80 % of total computation time [9].

Third, near grain boundaries the probe often samples overlapping regions of adjacent grains, producing superposed or mixed diffraction patterns that traditional template-matching cannot disentangle. When the misorientation between grains is small or the boundary is narrow, mixed patterns may be erroneously indexed as a single orientation, resulting in mislocated or missed boundaries [10].

1.2.2 Substrate-Selection Complexity in Polycrystalline and Multiphase Materials

Accurate selection of substrate (basis) templates is critical in analyzing polycrystals or multiphase materials, yet real specimens frequently comprise multiple phases, subgrains with subtly varying orientations, or strong texture gradients. This complexity poses severe challenges for template library construction—particularly for novel alloys and multiphase composites. First, different phases (e.g., austenite and ferrite in steel) may yield diffraction patterns that differ only

subtly, making it difficult to choose representative basis templates [11]. Second, in regions exhibiting continuous orientation gradients (such as deformation or subgrain boundaries), diffraction patterns vary continuously rather than corresponding to discrete orientations, so a single template cannot capture the full range of local patterns [12]. Finally, experimental variations—such as temperature fluctuations, beam-induced damage, or uneven sample thickness—can distort diffraction signatures, further complicating template matching and underscoring the need for more robust, automated boundary-detection methods [13].

1.2.3 Challenges in Grain-Boundary Identification and Triple-Junction Treatment

In transmission electron microscopy (TEM) and its derivatives—four-dimensional scanning TEM (4D-STEM) and scanning precession electron diffraction (SPED)—high-precision grain-boundary localization still faces substantial challenges. Compared to conventional SEM-EBSD, TEM-based orientation mapping offers nanometer-scale spatial resolution, yet diffraction signals near a boundary often originate from overlapping contributions of adjacent grains. Such signal mixing reduces the reliability of orientation indexing. For example, when diffraction spots from two grains overlap at a boundary, template-matching algorithms exhibit markedly lower confidence scores in the reliability map—boundary pixels appear darker, indicating increased uncertainty. This overlap complicates exact boundary determination, frequently necessitating compensation via neighboring-pixel information or post-processing algorithms [14]. Moreover, finite probe size and scan step increments constrain spatial precision: if the step size approaches the true boundary width, narrow grains may be “skipped”, or ultra-thin boundaries may be misidentified as broader bands. Likewise, when misorientation angles between grains lie near the chosen threshold (e.g., the 15° criterion separating high-angle boundaries from subboundaries), boundary detection becomes ambiguous. Taken together, these factors demand careful selection of criteria—such as critical misorientation thresholds and inter-pixel correlation metrics—to avoid false positives or missed boundaries in high-resolution orientation maps.

ASTAR has achieved success in nanocrystalline orientation measurement but also reveals precision limitations in boundary regions. ASTAR indexes diffraction patterns by template matching; however, in zones exhibiting high symmetry or multiple valid indexing solutions,

orientation ambiguities and misindexing frequently occur. Rauch et al. have shown that regions with 180° rotational symmetry can generate indexing ambiguities, producing spurious "pseudo-boundaries" within a single grain. These artifacts arise when a 180° misassignment yields an apparent misorientation above the threshold, causing isolated pixels to be falsely labeled as boundary segments. To address this, neighborhood-propagation ambiguity-correction algorithms replace suspect indices with the most reliable neighboring solutions, thereby suppressing false boundaries [15]. Nonetheless, even with such corrections, indexing near true boundaries may remain unstable, disrupting boundary continuity: orientation maps often display serrated or disconnected boundary lines, the result of neighboring-pixel misassignments or indexing gaps. Triple junctions (three-grain intersections) pose an even greater challenge for reliable boundary detection. A schematic illustration of a triple junction is shown in Fig. 1.5, which simply depicts the intersection point of three distinct grains. In practical diffraction-based indexing, however, diffraction signals from these three adjoining domains can overlap or compete during pattern matching, leading to unstable or erroneous solutions. Such effects may manifest as interrupted or misaligned junction lines, or even the appearance of spurious subgrain patches in the orientation map [16]. Thus, although ASTAR enhances orientation resolution, its precision in boundary localization—especially in complex topologies such as triple junctions—remains inadequate, necessitating further algorithmic improvements to achieve more robust boundary detection.

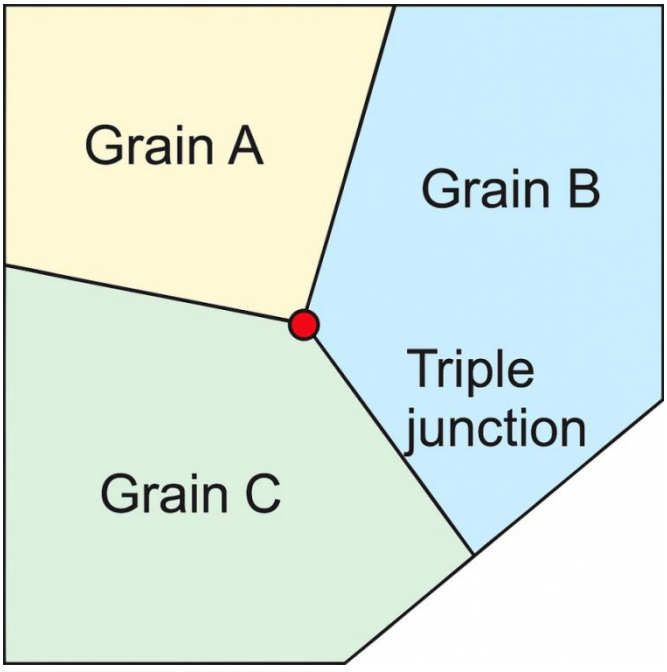

Fig. 1.5 Schematic illustration of a triple junction.

Direct identification of boundaries in TEM bright-field images or orientation maps likewise suffers from blurred edge and transition-zone issues. Contrast formation in TEM images is complex, and true boundaries often appear as gradual intensity gradients rather than sharp transitions, complicating automatic edge detection. For instance, Wei et al. demonstrated in Cu/V nanolamellar multilayers that deformation-induced interfacial transition zones appear as diffuse gray bands in high-resolution TEM, rather than crisp black-and-white boundaries, directly illustrating how adjacent grains can exhibit similar gray levels due to thickness and orientation variations. An example TEM image illustrating this is shown in Fig. 1.6, adapted from Wei et al. [17]. In another representative example, Feng et al. analyzed a ZrO_2 Σ9 model grain boundary using STEM-EDS and revealed a chemically and structurally complex boundary region, where signal mixing and gradual transitions hinder precise boundary definition. A corresponding STEM-EDS map is shown in Fig. 1.7, adapted from Feng et al. [18]. Coupled with imaging artifacts and noise, such phenomena limit conventional gradient-based edge detectors and often force reliance on manual tracing under high-contrast conditions—a time-consuming and subjective process. Consequently, whether using raw TEM images or orientation-mapping data, automatic grain-boundary extraction remains constrained by image blurring, signal mixing, and transition-zone ambiguity—challenges that must be overcome to achieve fully automated three-dimensional boundary reconstruction.

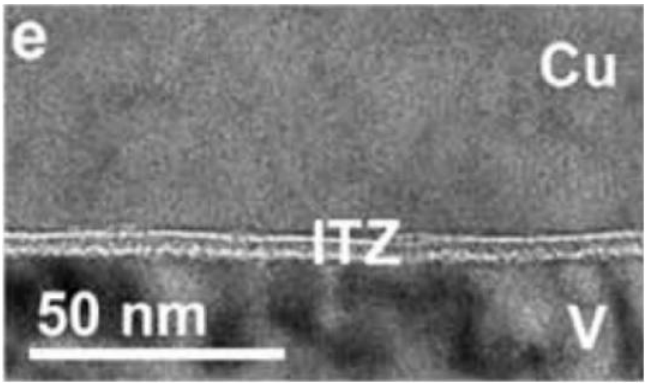

Fig. 1.6 Interfacial transition zone (ITZ) between Cu and V layers in CARBed Cu/V multilayers. (Adapted from Wei et al. [17], original Fig. 1(e)).

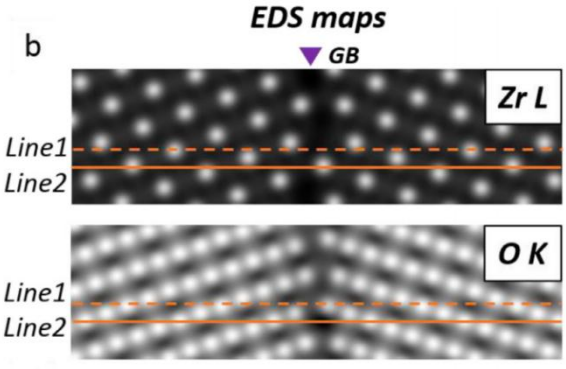

Fig. 1.7 Simulated STEM-EDS maps for Zr-L and O-K from the Σ9[110]/(221) grain boundary model. (Adapted from Feng et al. [18], original Fig. 2(b)).

1.3 Objectives of This Study

Based on the above background and current status, this study aims to propose an automatic grain-boundary detection method (see Section 1.1 and Fig. 1.3 for the definition of "boundary detection" as the extraction of an accurate 2D projection of the boundary) that does not rely on a template library and is based on constrained optimization and clustering. Unlike ASTAR, which requires point-by-point template matching, our method directly leverages differences in the grayscale distribution of diffraction images to group regions with similar diffraction patterns via clustering analysis, thereby identifying grains and grain boundaries without prior indexation.

In this study, "clustering" refers to an unsupervised classification process in which data points with similar features are grouped together. Each measurement point is represented by a three-dimensional weight vector obtained from the Optimize step, where the diffraction pattern of each pixel is decomposed into a linear combination of ASTAR-derived basis patterns. A similarity metric (e.g., Euclidean distance between these weight vectors) is calculated between points, resulting in a similarity graph. Based on this graph, a spectral clustering procedure is applied: a Laplacian matrix is constructed, its eigenvectors are computed to obtain a spectral embedding, and then k-means is performed on the embedded space to assign cluster labels. The resulting cluster assignments directly form the grain-boundary map. Through this process, pixels within the same crystalline grain exhibit similar weight-vector features and therefore fall into the same cluster, whereas pixels across a boundary show distinct weight-vector features and are separated into different clusters. This clustering-based approach fundamentally differs from template-matching methods such as ASTAR. Instead of attempting to index each point individually against a library, it infers grain regions and boundaries from the collective distribution of pattern features, which allows robust identification even when individual diffraction patterns are blurred or difficult to index.

This method offers several notable advantages: first, it automatically handles complex boundary topologies, including multi-grain intersections. At triple junctions, clustering analysis naturally divides the region into three grain categories without additional measures, whereas traditional methods require separate fitting for each grain pair, which is cumbersome and error prone. Second, the algorithm is efficient: clustering classifies the entire region in one pass, without

point-by-point matching or segment-by-segment fitting, making it advantageous for large datasets. Third, since no reference crystal templates are needed, the method reduces dependence on prior material information and has greater universality (e.g., it can be applied to unknown phases or poorly resolved diffraction patterns). Finally, the set of boundary points produced by this method creates the basis for subsequent three-dimensional reconstruction: by pairing boundaries extracted from different viewpoints—such as via stereoscopic imaging—the three-dimensional morphology of the boundaries can be reconstructed. This will be explored in future work.

1.4 Structure of This Thesis

The arrangement of the subsequent chapters is as follows:

Chapter 2 introduces the theoretical principles underlying this study, including the fundamental definition and structural characteristics of grain boundaries, basic knowledge of electron microscopy, methods for acquiring diffraction-image data, and the definitions of distance metrics for diffraction-pattern similarity and the principles of clustering. This discussion provides the theoretical foundation for the methods implemented in later chapters.

Chapter 3 describes the specific research methods and implementation steps. It first explains the experimental acquisition and preprocessing of 4D-STEM scanning diffraction data, then details the clustering–based grain-boundary detection algorithm, including the construction of the similarity matrix, Laplacian eigen decomposition, clustering classification, and special treatments and constrained-optimization strategies for triple-junction regions (e.g., ensuring connectivity of clustering results). This chapter also outlines the data structures and key parameter settings used in the algorithm implementation. In addition, this chapter also introduces the design of quantitative validation based on cosine similarity profiles, describing how sampling lines are defined across boundaries and how feature-vector similarities are computed to support later evaluation.

Chapter 4 presents the experimental results and detailed analysis of the proposed grain-boundary detection method. Actual 4D-STEM datasets from selected material regions were processed, and the constrained-optimization-based diffraction-pattern decomposition and clustering workflow was applied to generate two-dimensional grain-boundary maps. To ensure the reliability of these results, the primary validation was performed through diffraction-pattern superposition measurements, directly examining diffraction spots at grain-boundary regions and confirming the physical consistency of detected boundaries. Beyond these qualitative checks, this chapter further presents quantitative validation results. Cosine-similarity profiles along five sampling lines are analyzed to reveal a clear high–low–high trend when crossing gray-band regions, directly demonstrating that the detected boundaries isolate transition zones while maintaining feature consistency within grains. In addition, the extracted boundaries were quantitatively compared with

those obtained from ASTAR and ASTAR + MLS methods, focusing on metrics such as the average deviation of detected boundaries from manually annotated references, the statistical distribution of boundary-width variations, and the continuity of boundary segments across triple junctions. The results show that the proposed method yields smaller boundary deviations, exhibits more stable boundary widths, and maintains higher boundary continuity, particularly in complex regions such as triple junctions.

Chapter 5 concludes the work by summarizing the improvements and significance of the proposed method in grain-boundary detection. It also discusses remaining limitations and challenges and outlines prospects for future research, including applications in more complex material systems, integration with advanced machine-learning optimizations, and three-dimensional reconstruction of grain boundaries.

Chapter 2 Principles

2.1 Crystalline Grain Boundaries

Crystalline grain boundaries are interfaces between adjacent grains in polycrystalline materials, i.e., boundaries where the crystal orientations differ on either side [19]. As a two-dimensional crystal defect, the lattice arrangement at the grain boundary is mismatched and disrupted, often containing dense dislocations, steps, and other defect structures. Depending on the magnitude of the orientation difference between the two grains, grain boundaries are classified as low-angle or high-angle: typically, when the misorientation between grains is less than approximately 15°, it is considered a low-angle grain boundary, whose structure can be viewed as an array of regularly spaced dislocations accommodating the small orientation difference; when the misorientation exceeds 15°, it is categorized as a high-angle grain boundary, wherein the interface becomes more disordered and cannot be described by a simple dislocation model [20].

The presence of grain boundaries significantly influences the mechanical, electrical, and other properties of materials. On one hand, grain boundaries obstruct dislocation motion, thereby increasing material strength, which is the basis of the well-known Hall–Petch effect: the yield strength of a material increases as grain size decreases. Hall and Petch experimentally elucidated this grain refinement strengthening relationship in 1951 and 1953, respectively, and their empirical formula is:

$$\sigma_d = \sigma_0 + \frac{k}{\sqrt{d}} \quad \#(2\text{-}1)$$

where d is the grain size, σ_d is the stress at yield or a flow stress at higher plastic strains, σ_0 is the corresponding stress for large single crystals or very large grained material (we refer to it here as the bulk stress), and k is a constant that may be predicted by theory or may be considered to be a material constant [21]. As grains become smaller, the number of grain boundaries per unit volume increases, and the barriers that dislocations must overcome at grain boundaries multiply, leading to an increase in yield strength. On the other hand, lattice disorder and atomic bond defects at grain boundaries also interrupt electron and phonon transport pathways, causing grain boundaries to

reduce electrical conductivity and thermal conductivity. For example, in polycrystalline semiconductor thin films, excessive grain boundaries increase carrier scattering rates and raise resistivity [22]. Furthermore, grain boundaries possess high interfacial energy, tend to be sites for elemental segregation and second-phase precipitation, and may become initiation sites for corrosion and crack nucleation [23]. All of these factors make grain boundary engineering—through the control of grain boundary number, distribution, and structure—an important means of optimizing material properties.

The geometrical crystallography of grain boundaries is usually described by the orientation of the boundary plane and the misorientation (angular difference) between the two grains. In high-angle grain boundaries, due to the large misorientation, atomic arrangements at the interface are highly mismatched, and the interfacial atomic structure often appears disordered or consists of complex periodic structural units, whereas low-angle grain boundaries can be regarded as arrays of discrete dislocations, and low-angle tilt boundaries can be viewed as networks of screw dislocations. As misorientation increases, these dislocations on the interface gradually approach and interact, and when θ exceeds a critical value (approximately 10°–15°), the crowded dislocations at the interface cause a complete mismatch of atomic arrangements, thus transitioning to a high-angle grain boundary state. Some high-angle grain boundaries can be described using the coincidence site lattice (CSL) model to represent their approximate ordering, using the Σ value to characterize the lattice coincidence relationship across the boundary—smaller Σ values indicate a higher degree of lattice coincidence and therefore relatively lower interfacial energy, whereas general high-angle boundaries without special orientation relationships exhibit higher interfacial energy [24]. In summary, crystalline grain boundaries, as significant defects in crystalline materials, profoundly affect material properties through their structure and distribution.

2.2 Electron Tomography

Electron tomography is a technique that utilizes transmission electron microscopy (TEM/STEM) to acquire three-dimensional structural information of a specimen. Its principle is analogous to medical CT scanning: by tilting the sample and collecting a series of two-dimensional projection images at different angles (typically within a ±60–70° range, with fixed angular increments to acquire several dozen projections), one then employs computational reconstruction algorithms (such as weighted back-projection or algebraic iterative reconstruction) to synthesize these tilted projections into a three-dimensional volume reconstruction of the sample. Because a single TEM image represents a two-dimensional superimposed projection along the line of sight, there exists a “shadowing effect” caused by overlapping depth information; electron tomography compensates for this limitation through multi-angle projections, enabling nanoscale three-dimensional visualization. Since the introduction of electron-tomography techniques in the 1960s, the method has been used in the life sciences for three-dimensional reconstruction of cellular ultrastructure and, since the 1990s, has gradually been adopted in materials science. Today, approaches such as Z-contrast HAADF-STEM tomography and energy-filtered tomography allow acquisition of three-dimensional morphology and compositional distribution of materials at the nanoscale or even atomic scale [25]. It should be noted that, due to instrument limitations, electron tomography typically cannot achieve a full 180° tilt range, resulting in a “missing wedge” of information in the reconstruction data, which reduces resolution perpendicular to the tilt axis. Furthermore, constraints on electron-beam dose and sample drift limit the number and quality of obtainable projections. Therefore, optimizing tilt schemes, aligning projection images, and adopting advanced reconstruction algorithms (such as compressed sensing or ART) remain key research directions for improving tomographic reconstruction accuracy.

2.3 Transmission Electron Microscopy

Transmission Electron Microscopy (TEM) employs a high-energy electron beam, typically accelerated at 100–300 kV, to illuminate an ultrathin specimen; electrons transmitted through the sample are imaged via electromagnetic lenses to obtain high-resolution micrographs of the specimen's internal structure. Fig. 2.1 illustrates a schematic of the TEM's electron-optical pathway, including the electron gun, condenser lens system, objective lens, intermediate lens, and projection lens. Due to the extremely short de Broglie wavelength of electrons (for example, ~0.0025 nm at 200 kV), far below the wavelength of visible light, TEM theoretically offers much higher resolution than optical microscopy. Modern high-resolution TEM, coupled with aberration correctors, can directly image atomic columns of crystal lattices under point-resolution conditions [26].

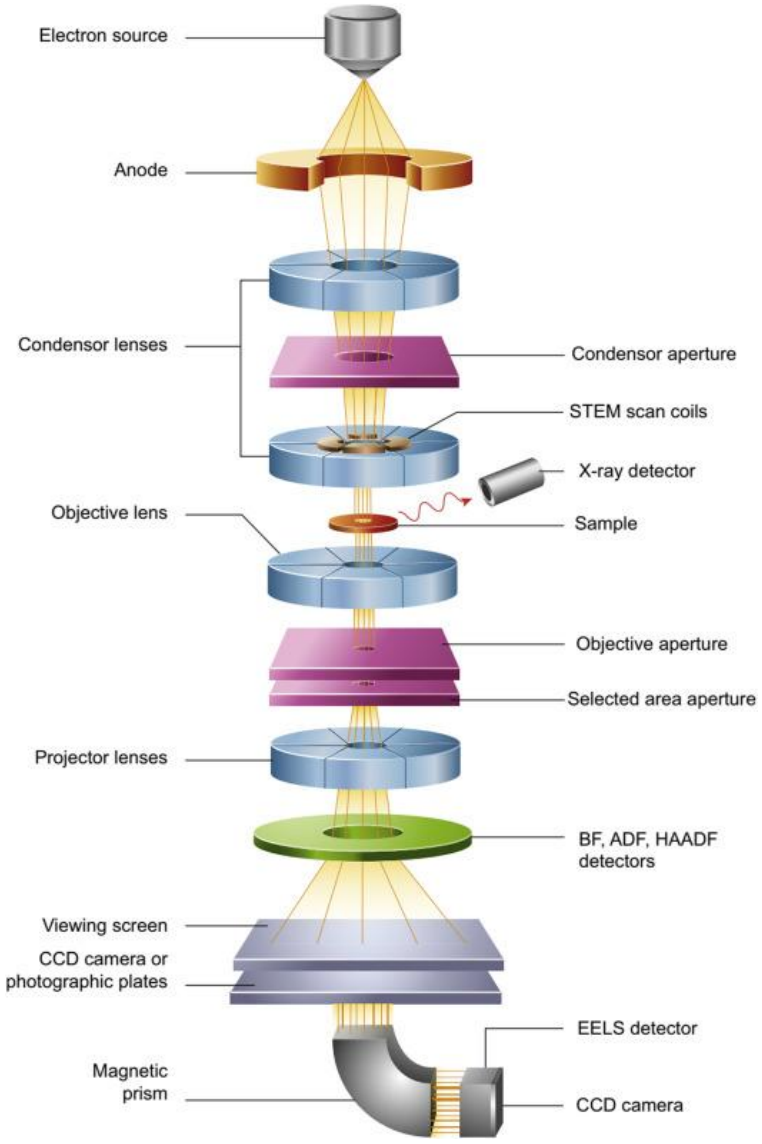

Fig. 2.1 Schematic of electron-optical imaging in a transmission electron microscope. A focused high-energy electron beam transmits through a thin sample, forming a diffraction pattern (reciprocal space) at the objective back focal plane and a real-space image at the objective imaging plane. By selecting different imaging planes and magnifying with the intermediate lens, one can observe either diffraction patterns or magnified real-space images on the screen.

TEM supports multiple imaging modes: by switching between the objective and intermediate lenses, one can acquire real-space images (bright-field, dark-field, etc.) or reciprocal-space electron diffraction patterns. In conventional imaging modes, the zero-order transmitted beam and selected diffracted beams at the objective back focal plane are chosen by the objective aperture and imaged to produce bright-field images (contrast primarily from mass-thickness variations) or dark-field images (highlighting crystal regions satisfying specific diffraction conditions). By adjusting the intermediate lens to image the objective back focal plane, one can directly obtain electron diffraction patterns for crystallographic analysis (see Section 2.4). Because electrons interact strongly with matter, TEM imaging imposes stringent requirements on specimen thickness and condition: specimens must be sufficiently thin (below tens of nanometers) to ensure adequate electron transmission and are typically prepared as ~3 mm diameter foils or cross-sections mounted on copper grids. In this study, we used TEM to obtain high-resolution images and selected-area electron diffraction of regions containing grain boundaries, aiding in the analysis of boundary orientation relationships and structures [27].

As a transmission imaging technique with an extremely small probe size, TEM can directly reveal atomic arrangements and interfacial structures at grain boundaries. However, due to strong electron–matter interactions, thick specimens introduce multiple scattering effects that complicate contrast interpretation. Additionally, electron-beam irradiation can induce sample damage; therefore, a balance between accelerating voltage and beam current is required to achieve high signal-to-noise images while minimizing damage. In this study, we employed a 200 kV TEM to image grain boundary regions, ensuring high resolution while reducing sample damage, thereby providing clear direct images for boundary structure analysis [28].

2.4 Electron Diffraction

Electron diffraction is a technique that exploits the interference of high-velocity electron waves with the periodic atomic array of a crystal to obtain structural information. Its physical basis is analogous to X-ray diffraction, both obeying Bragg's law.

$$n\lambda = 2d\sin\theta \quad \#(2\text{-}2)$$

In TEM, when a parallel electron beam transmits through a thin crystalline film, each atomic plane diffracts the electrons into a series of beams satisfying the Bragg condition. On the phosphor screen, these beams form a regularly spaced pattern of diffraction spots, known as an electron diffraction pattern. Because the electron wavelength at typical accelerating voltages is over two orders of magnitude shorter than that of X-rays, the diffraction angles are usually only a few degrees or less, resulting in widely spaced spots that allow observation of multiple higher-order reflections on a limited-size screen. Another characteristic of electron diffraction is the strong interaction between electrons and matter, so spot intensities depend not only on the crystal's geometric structure but also on multiple scattering effects; dynamic scattering must therefore be considered when interpreting intensities [29].

Simultaneously, electron diffraction is highly effective for localized analysis: using Selected Area Electron Diffraction, an aperture inserted in the image plane isolates electrons from a specific region of the specimen, yielding diffraction solely from that area and enabling local crystallographic and orientation analysis. For even smaller sampling volumes, a focused electron probe can acquire diffraction from regions on the order of tens of nanometers or less. Overall, electron diffraction offers direct information with relatively low instrument investment and, in this study, was employed to determine the misorientation between grains across boundaries [30].

A typical electron diffraction pattern comprises a central transmitted-beam spot surrounded by periodically arranged diffraction spots corresponding to lattice planes in reciprocal space. By measuring inter-spot spacings and angles, one can calculate interplanar distances and crystal symmetry, thereby determining lattice parameters and orientation. In thicker specimens or at larger orientation deviations, diffraction spots may elongate into alternating dark–bright lines (Kikuchi

bands), providing fine orientation details. In practice, experimental patterns are indexed by comparison with the known reciprocal lattice of the crystal structure, assigning Miller indices to the spots and confirming phase and orientation.

In electron diffraction, the intensity of each diffraction spot is, under the kinematical approximation, proportional to the square of the structure factor F_{hkl}, where F_{hkl} is defined as the sum of the scattering contributions from all atoms in the unit cell:

$$F_{hkl} = \sum_j f_j exp\left[2\pi i\left(hx_j + ky_j + lz_j\right)\right] \quad \#(2\text{-}3)$$

with f_j being the atomic scattering factor and (x_j, y_j, z_j) the fractional coordinates of atom j. This relationship allows one to qualitatively predict the relative brightness of diffraction spots in ideal thin samples. However, in practical specimens, the kinematical approximation breaks down due to dynamical effects, such as multiple scattering within thicker regions, channeling along specific crystal directions, and strong electron–crystal interactions. As a result, the observed spot intensities do not directly equal $\left|F_{hkl}\right|^2$, and interpretation becomes qualitative rather than purely quantitative.

To aid understanding of the electron diffraction mechanism, Fig. X illustrates the Bragg condition: when an incident electron beam interacts with a set of crystal planes with spacing d, constructive interference leads to diffraction spots at angles satisfying the Bragg condition (see Eq. 2-1). This basic principle forms the foundation for relating diffraction spot intensities to the structure factor under the kinematical approximation.

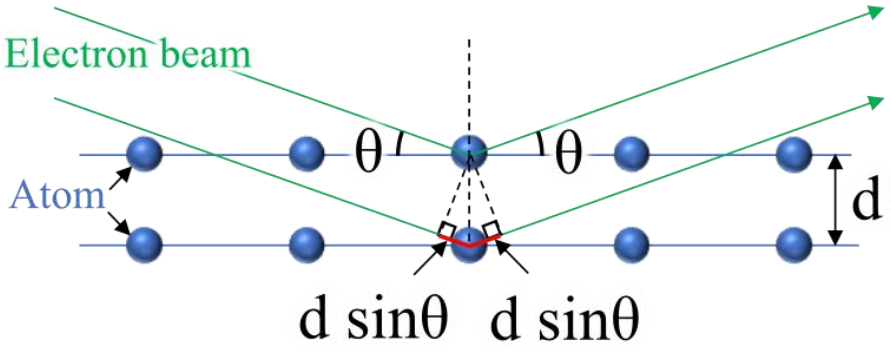

Fig. 2.2 Schematic diagram of electron diffraction.

2.5 NBED (Nano-Beam Electron Diffraction)

Conventional selected-area electron diffraction (SAED) is constrained by the diameter of the aperture, limiting analysis to micrometer-scale regions. As schematically illustrated in Fig. 2.3, SAED uses a relatively broad, parallel electron beam defined by a selected-area aperture, so the illuminated region on the specimen is large. In contrast, nano-beam electron diffraction (NBED) forms a finely converged probe, with a beam diameter reduced to a few nanometers—or even sub-nanometer—enabling diffraction collection from localized nanoscale volumes [31]. This focused configuration substantially reduces contributions from surrounding areas and improves spatial resolution for diffraction analysis. In an NBED experiment, the TEM illumination system is configured with a very small convergence semi angle so that a coherent, bright electron probe of nanometer-scale diameter is formed on the specimen. Because the sampling volume is correspondingly small, NBED can avoid interference from neighboring grain boundaries or dislocation networks and acquire diffraction patterns representative of a single grain domain, making it well suited for investigating local strain, grain orientation, and defect structures in nanocrystalline materials and thin films.

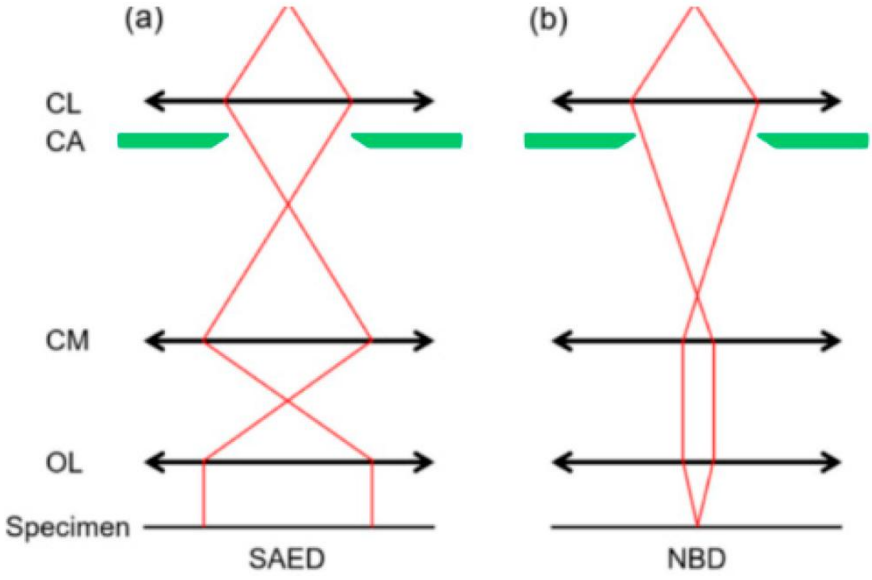

Fig. 2.3 Comparison of electron-beam configurations for different diffraction modes: (a) SAED, (b) NBD, and (c) CBED.

NBED has been applied to measure micro-scale strain, orientation, and defects: by analyzing a series of adjacent probe positions, one can map local variations in lattice parameters as relative

strain ($\Delta d/d$) with a precision on the order of 10^{-4} (dimensionless). This approach is also referred to as 4D-STEM strain mapping (see Section 2.7)—in STEM mode, a diffraction pattern is recorded at each probe position and the shift of diffraction spots is used to calculate the strain field. Moreover, by further reducing the probe size to the sub-nanometer regime, NBED can probe short-range order in amorphous materials [32]. It should be noted, however, that the high dose density inherent to a highly focused beam increases the risk of electron-beam damage, necessitating careful dose management. In this study, we employ the NBED mode within our 4D-STEM experiments: a nanometer-scale probe is scanned across the sample in STEM, and a diffraction pattern is recorded at each position to support grain-orientation clustering and boundary analysis.

2.6 PED (Precession Electron Diffraction)

Precession electron diffraction (PED), first introduced by Vincent and Midgley in 1994, is a technique for acquiring quasi-kinematic diffraction intensities by rocking the electron beam in a conical motion about the optical axis. During PED, the beam precesses at a fixed semiangle while traversing the specimen, averaging diffraction intensities over many incident directions. This averaging substantially reduces the effects of dynamical (multiple) scattering, so that the measured intensity of each diffraction spot approaches the intensity corresponding to the structure factor itself. In conventional electron diffraction without PED, dynamical effects cause the diffraction intensity to vary with excitation error s_g and specimen thickness, leading to oscillations and thickness fringes. These thickness fringes are a typical manifestation of dynamical scattering, arising from the interference between Bloch waves over an extinction distance. Under PED conditions, by integrating intensities over many incident directions, the influence of excitation error and thickness fringes is strongly suppressed, yielding intensities that more closely follow kinematical predictions. (A schematic showing excitation error, extinction distance, and the disappearance of thickness fringes under PED is recommended to be inserted here.) As a result, PED-derived intensities can be used for reliable three-dimensional structure solution and have successfully resolved complex crystal structures in electron crystallography. Over the past two decades, PED has evolved from a niche method into a cornerstone of electron crystallography [33].

PED is employed in two primary applications: (1) as a standalone crystallographic technique for structure determination via collection of quasi-kinematic intensities; and (2) in conjunction with scanning electron diffraction for automated orientation and phase mapping in TEM. Compared to conventional parallel-beam diffraction, PED spots are more symmetric, better defined, and exhibit lower background noise, thereby enhancing orientation discrimination and angular resolution. For example, implementation of a 1–2° precession angle in the ASTAR system has been shown to improve misorientation-angle precision to approximately 0.5°. Practical use of PED requires precise synchronization of beam deflectors and microscope lenses, often necessitating a dedicated precession-unit attachment. As schematically illustrated in Fig. 2.4, the PED optical system includes a pair of beam-deflection coils (precession coils) that tilt the incident electron beam off the optical axis by the chosen semiangle and then rotate it in a conical path around the axis. Downstream

projector lenses and deflectors are synchronized so that the diffracted beams are realigned onto a stationary diffraction pattern on the detector. This configuration enables the averaging of diffraction intensities over multiple incident directions while maintaining a stable diffraction geometry.

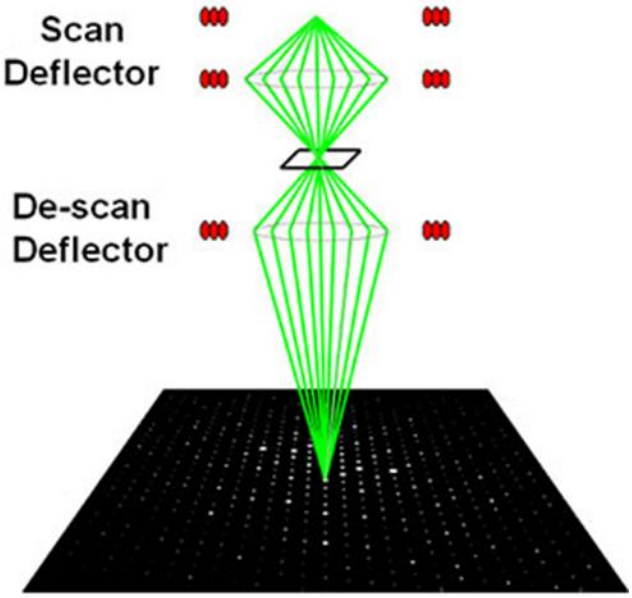

Fig. 2.4 Schematic of the PED optical system.

2.7 4D-STEM

Four-dimensional STEM (4D-STEM) refers to the acquisition of a full diffraction pattern at each probe position during a two-dimensional STEM scan, thus generating a four-dimensional dataset consisting of probe-scan coordinates (x, y) and diffraction coordinates (k_x, k_y) [34]. In conventional STEM, only a single intensity value (e.g., bright-field or annular-dark-field signal) is recorded per probe position; in 4D-STEM, a fast, pixelated detector captures the entire diffraction pattern, enabling “one-scan, multiple-contrast” imaging. Post-acquisition, virtual detectors can be defined in software to integrate different regions of reciprocal space—for example, summing the central diffraction disk yields a virtual bright-field image, while integrating high-angle scattered electrons produces an annular-dark-field image [35].

Beyond imaging, each recorded diffraction pattern can be analyzed by pattern-matching or template-matching algorithms to determine local crystal orientation or phase, producing orientation and phase maps with spatial resolution down to tens of nanometers or better—surpassing SEM-EBSD and being largely insensitive to sample thickness variations. Moreover, 4D-STEM data can be exploited for ptychographic phase retrieval to break the resolution limit imposed by lens aberrations, enabling super-resolution imaging under low-dose conditions [36]. Correlation analyses of diffraction patterns can also yield three-dimensional structural insights or pinpoint defects.

Thanks to advances in high-speed direct-electron detectors and big-data processing, 4D-STEM has become a forefront technique in TEM. In this study, we use 4D-STEM to acquire diffraction datasets encompassing grain-boundary regions and subsequently apply computational clustering to extract grain orientations and identify boundaries. It should be noted that the large data volumes necessitate careful optimization of probe size, camera length, and processing pipelines to balance signal-to-noise ratio and spatial resolution.

2.8 4D-SPED

Four-Dimensional Scanning Precession Electron Diffraction (4D-SPED) merges 4D-STEM with PED by precessing the beam at each probe position during the scan and recording the integrated diffraction pattern. This hybrid approach leverages the high-throughput orientation-mapping capability of 4D-STEM and the quasi-kinematic benefits of PED. In a 4D-SPED experiment, the beam is precessed by a small angle for each probe position, and the detector accumulates diffraction intensities over the precession cycle. By averaging out dynamical scattering effects, the resulting patterns exhibit clear, kinematic-like spots that can be reliably used for template or pattern matching, where the template diffraction patterns are pre-calculated from crystallographic data based on structure factors (i.e., the amplitude of each diffraction spot is derived from the square of the corresponding structure factor under the kinematical approximation), thereby achieving high-precision orientation determination. The overall SPED acquisition process is schematically shown in Fig. 2.5.

Jeong et al. demonstrated that PED-assisted 4D-STEM reduces indexing errors to below 1% when using high-speed CMOS detectors, and that additional measures—such as blocking the direct beam—can further enhance angular resolution to sub-1°, enabling detection of subgrain and small-angle boundaries akin to Kikuchi-pattern EBSD [37]. In our work, we employ the ASTAR platform configured for 4D-SPED: each diffraction pattern is matched against a precomputed template library to automatically map grain orientations and facilitate robust boundary identification in complex polycrystalline materials.

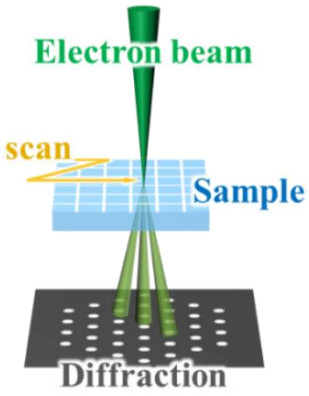

Fig. 2.5 Schematic diagram of the SPED acquisition mode.

2.9 ASTAR Method

The ASTAR technique, commercialized by NanoMEGAS in 2006, is a TEM-based orientation-mapping and phase-mapping method analogous to SEM-EBSD but offering approximately an order of magnitude higher spatial resolution (down to the nanometer scale) and superior discrimination of multiphase, fine-scale orientations. In ASTAR, the electron beam is focused into a probe roughly 2 nm in diameter to raster across the specimen and acquire diffraction patterns comparable to those used in EBSD.

To mitigate intensity variations in the diffraction spots caused by slight specimen bending or strain, ASTAR employs scanning precession electron diffraction (SPED). Diffraction patterns are collected using NanoMEGAS's proprietary TopSpin software in SPED mode, which ensures stable, high-quality image acquisition. The collected patterns are then indexed, phase-identified, and orientation-calculated via a patented template-matching algorithm. Templates are generated by simulating all possible diffraction patterns on a pole-figure grid at approximately 1° orientation increments, based on the sample's crystal structure, accelerating voltage, and detector geometry.

By matching each measured diffraction pattern against this template library, ASTAR produces nanometer-resolution orientation and phase maps. The method has been widely applied in materials science to characterize texture and grain-orientation distributions in metals, identify new or metastable phases, and observe phase-boundary migration during strain-induced transformations. In the present study, we utilized ASTAR to map the crystal orientations in regions adjacent to grain boundaries. These maps enable direct visualization of orientation changes across boundaries and serve as a benchmark for our subsequent diffraction-pattern clustering analyses. Additionally, ASTAR mapping facilitates detection of minor grains or secondary-phase inclusions whose orientations deviate markedly from the matrix, providing a comprehensive picture of the microstructure surrounding grain boundaries [38].

2.10 K-means clustering

K-means is a classical and widely used unsupervised clustering algorithm that aims to partition a set of data points into a predefined number of clusters, denoted as k. The objective of K-means is to minimize the within-cluster variance, which is equivalent to minimizing the sum of squared Euclidean distances between each data point and the centroid of the cluster to which it is assigned.

The algorithm operates iteratively. It starts by selecting k initial centroids, which can be chosen randomly or by other initialization strategies. Each data point is then assigned to the cluster whose centroid is nearest in terms of Euclidean distance. After the assignment step, the centroids are recomputed as the mean position of all data points within each cluster. These two steps—assignment and centroid update—are repeated until the centroids stabilize or a convergence criterion is met.

K-means is computationally efficient and works well when clusters are roughly spherical and of similar size, making it a fundamental method in many data analysis and pattern recognition tasks.

For clarity, Figure 2.6 shows a simple illustrative example: eight sample points are embedded in a 2D space by the first two eigenvectors of L and grouped into three clusters using k-means; colors indicate cluster labels, which are then assigned back to the original nodes in the graph.

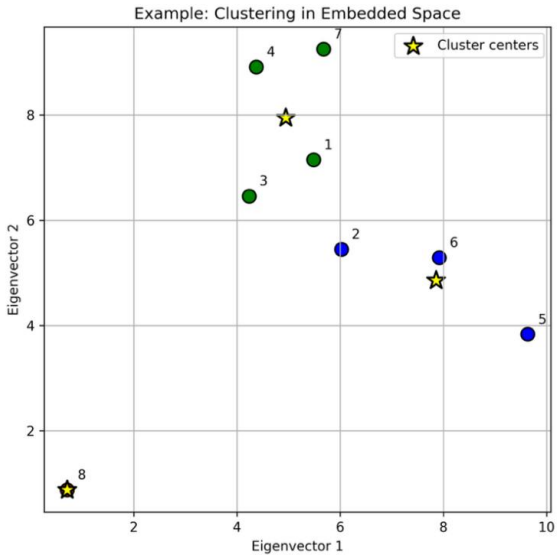

Fig. 2.6 Example of K-means clustering in embedded space.

Chapter 3 Methods

This chapter describes in detail the experimental methods and procedures used in this study. First, the acquisition and preprocessing of 4D-STEM scanning precession electron diffraction data are explained. Next, the grain-boundary detection algorithm based on clustering is presented, including the construction of the similarity matrix, eigen decomposition of the Laplacian matrix, clustering classification, and the special treatment and constrained-optimization strategy for triple-junction regions. Finally, the methods for validation of the extracted grain boundaries are introduced.

3.1 4D-SPED Data Acquisition

3.1.1 Sample Preparation

An austenitic stainless steel (SUS316L) was chosen as the experimental material. This alloy has low carbon content and typical composition of 16–18% Cr, 12–15% Ni, and 2–3% Mo, offering excellent corrosion resistance and mechanical properties. Specimens were mechanically polished and thinned by focused-ion-beam (FIB) to a TEM foil thickness of several tens of nanometers, ensuring electron transparency (see Fig. 3.1). Under an optical microscope, the prepared foil shows an equiaxed polycrystalline structure with average grain size of about 1 μm. A region containing multiple grain-boundary intersections was selected for scanning analysis.

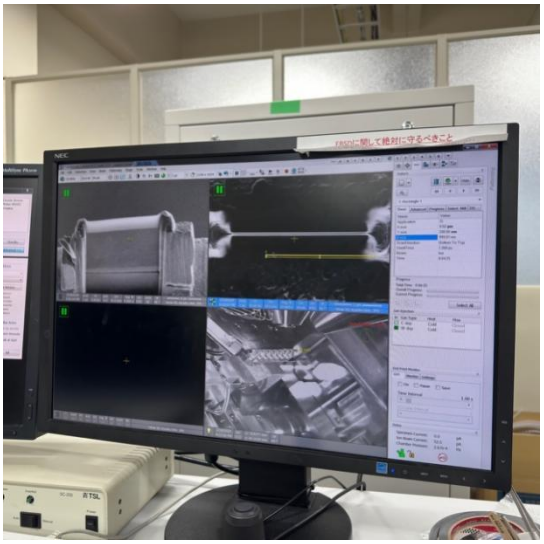

Fig. 3.1 The process of sample preparation using FIB

3.1.2 4D-SPED Scanning

To obtain both intra-grain and boundary diffraction information, scanning precession electron diffraction (SPED) in 4D-STEM mode was used. Experiments were performed on a JEOL ARM-200F field-emission TEM at 200 kV. The data acquisition conditions are shown in Table 3.1. A double-tilt holder enabled data collection at different tilt conditions: first at alpha=0° (untilted) to acquire the first 4D-STEM dataset, then tilted by 20° about the alpha axis to acquire the second dataset. These yielded two datasets from different viewpoints, denoted alpha 0° and alpha 20°. The scan area covered approximately 2.3 μm × 2.3 μm with a step size of 6 nm, producing 386 × 386 diffraction patterns per dataset. Regions of interest were then cropped to image sizes of 225 × 137 (alpha=0°) and 207 × 136 (alpha=20°) pixels. To mitigate effects of thickness variation and dynamical diffraction, beam precession was enabled in SPED mode with a precession angle of 0.5° and four precession cycles per scan. This produced more uniform and stable diffraction-spot intensities, advantageous for subsequent analysis. A schematic of the SPED mode is shown in Fig. 3.2.

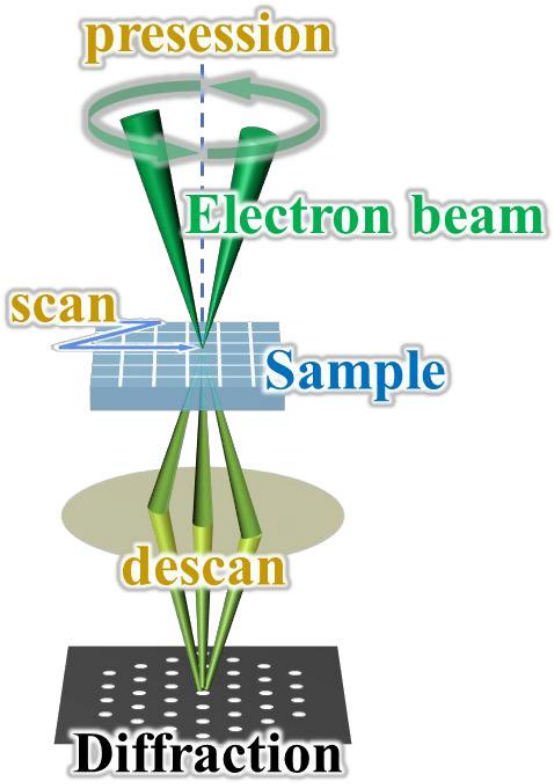

Fig. 3.2 SPED mode diagram

During acquisition, NanoMEGAS TopSpin software controlled scanning and recorded diffraction data in real time. Each tilt dataset was saved as a block file (4D-STEM proprietary format) containing all diffraction images and metadata. Block files were read with HyperSpy and diffraction patterns batch-exported to standard image formats. During export, original 16-bit grayscale patterns were downscaled to 8 bit to reduce storage. Each tilt's images were preliminarily aligned using vacuum regions as references to enable multi-viewpoint registration. Virtual bright-field images for each tilt are shown in Fig. 3.3.

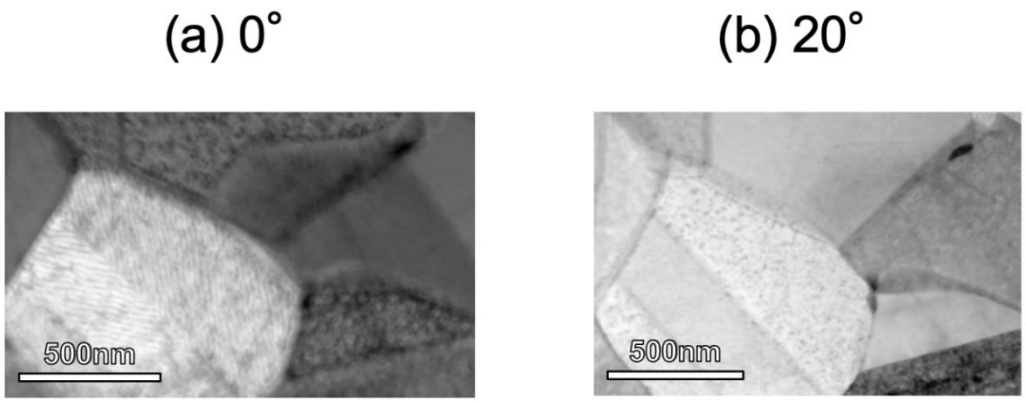

Fig. 3.3 Virtual bright-field images for each tilt dataset

Table 3.1 Data acquisition conditions

Equipment	ARM-200F（JEOL）
TEM holder	double-tilt holder（JEOL）
Image acquisition mode	TEM-SPED
Acceleration voltage [kV]	200
Sample	SUS316L
Tilt angle [°]	0, 20
Step Interval [nm/pixel]	6
Camera Length[cm]	30
Precession frequency	4

3.2 Crystal Orientation Mapping by ASTAR Method

The acquired 4D-SPED data were input to the ASTAR system for crystal-orientation analysis. NanoMEGAS Index2 software was used to index the alpha=0° and alpha=20° datasets. First, experimental parameters (200 kV acceleration voltage, illumination mode, camera length, etc.) were entered into NanoMEGAS DefGen2 software and a CIF file containing crystal-system information was imported to generate a diffraction-pattern template library. This template library (.bnq) comprises simulated patterns at 1° orientation increments covering all possible orientations. Next, the template library and experimental block files were imported into Index2, and diffraction patterns were indexed point by point by template matching to determine the crystal orientation at each scan position. Fig. 3.4 presents a color-coded orientation map of the region. Index2 also outputs a reliability map that quantifies confidence of each index; near grain boundaries, pattern overlap reduces matching confidence, appearing as darker regions on the reliability map. In the orientation map, pixels with orientation difference greater than 5° between adjacent points were marked as grain boundaries and highlighted in black. However, template matching in transition zones sometimes produced misindexing and orientation jumps, resulting in boundary interruptions or misalignments. In triple-junction regions, reliability dropped significantly, indicating that single-orientation templates could not match the mixed patterns. The limitations of this conventional approach in boundary localization will be addressed by improved algorithms in later chapters.

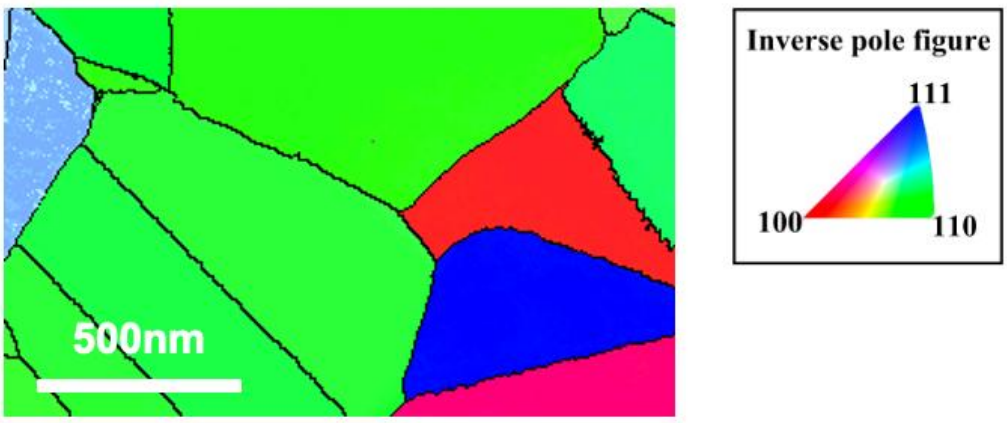

Fig. 3.4. Color-coded orientation map generated by ASTAR indexing.

3.3 Grain-Boundary Extraction

Figure 3.5 illustrates the overall workflow of the proposed grain-boundary extraction algorithm. The process begins with 4D-SPED data acquisition, including sample scanning, data export, and initial preprocessing. Next, ASTAR pre-processing is performed to generate preliminary grain masks, assign grain numbers, and obtain segmented regions. The algorithm then applies Optimize three-basis fitting to each pixel to obtain the weight vector [wA,wB,wC]. Based on these weight vectors, a similarity graph is constructed by computing the similarity matrix W and forming a weighted undirected graph. Afterward, feature vector embedding based on the graph Laplacian is carried out by computing the degree matrix and Laplacian matrix, extracting the first k eigenvectors, and forming the embedding space. Finally, K-means clustering is performed in the embedding space to assign cluster labels to pixels, completing the grain-boundary detection workflow.

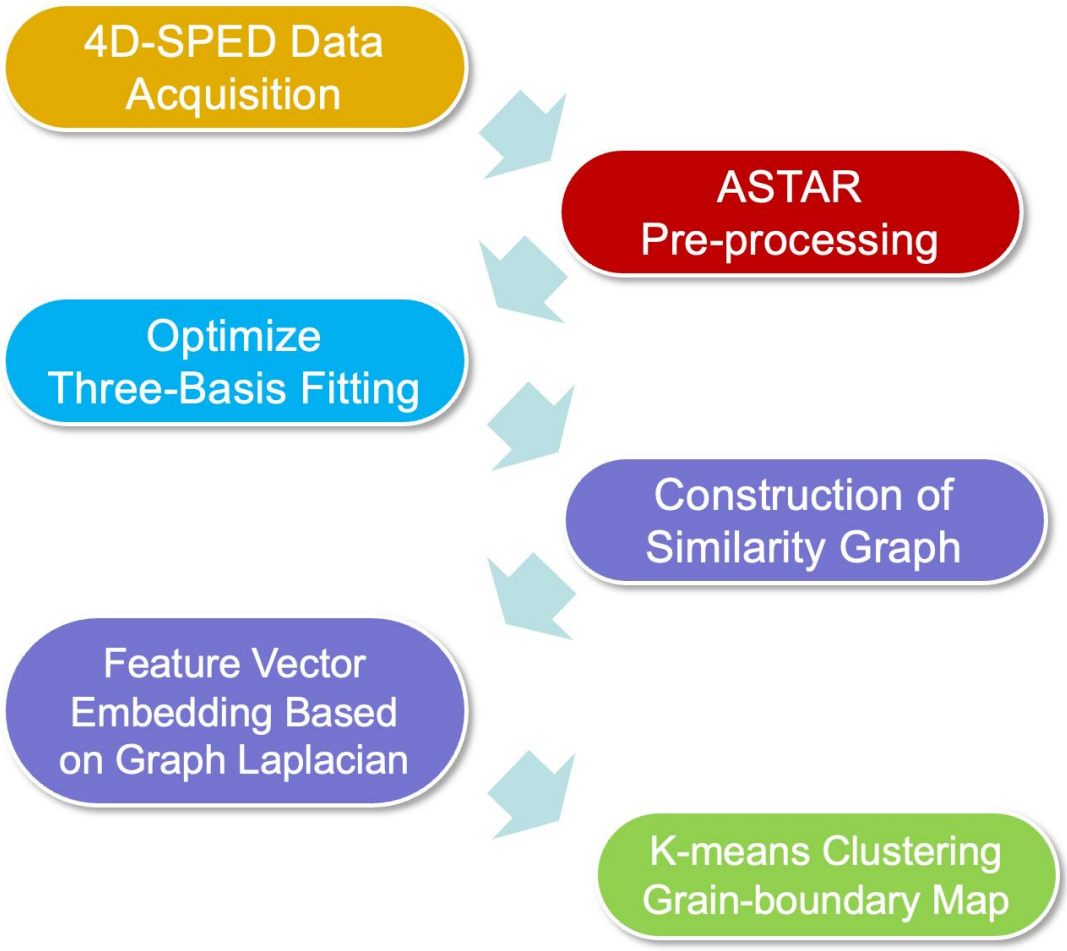

Fig. 3.5 Overall workflow of the proposed grain-boundary detection method.

3.3.1 Generation of Grain-Mask Images and Grain Numbering

From the ASTAR orientation distribution, binary mask images for each grain were generated and unique labels assigned. Specifically, major grains in the analysis region were selected, ignoring edge regions that were too thin or islands whose orientations were too complex. In the orientation map, OpenCV's findContours function extracted contours of each grain. Each grain interior was filled with white (pixel value 255), while background and non-grain regions remained black (pixel value 0), yielding binary masks for each grain. Fig. 3.6 shows the binary masks. Because grain boundaries in the orientation map have finite pixel width, those pixels were assigned to background (black) in the mask, leaving only grain interiors. Next, a grain-label image was created: for each mask, white pixels were assigned the grain's label in the label image, while other pixels remained 0. Fig. 3.7 shows example grain-label images, where different gray levels denote different grain labels and 0 indicates boundary or background. This one-to-one labeling of grains provides the data structure needed for subsequent grain-boundary analyses.

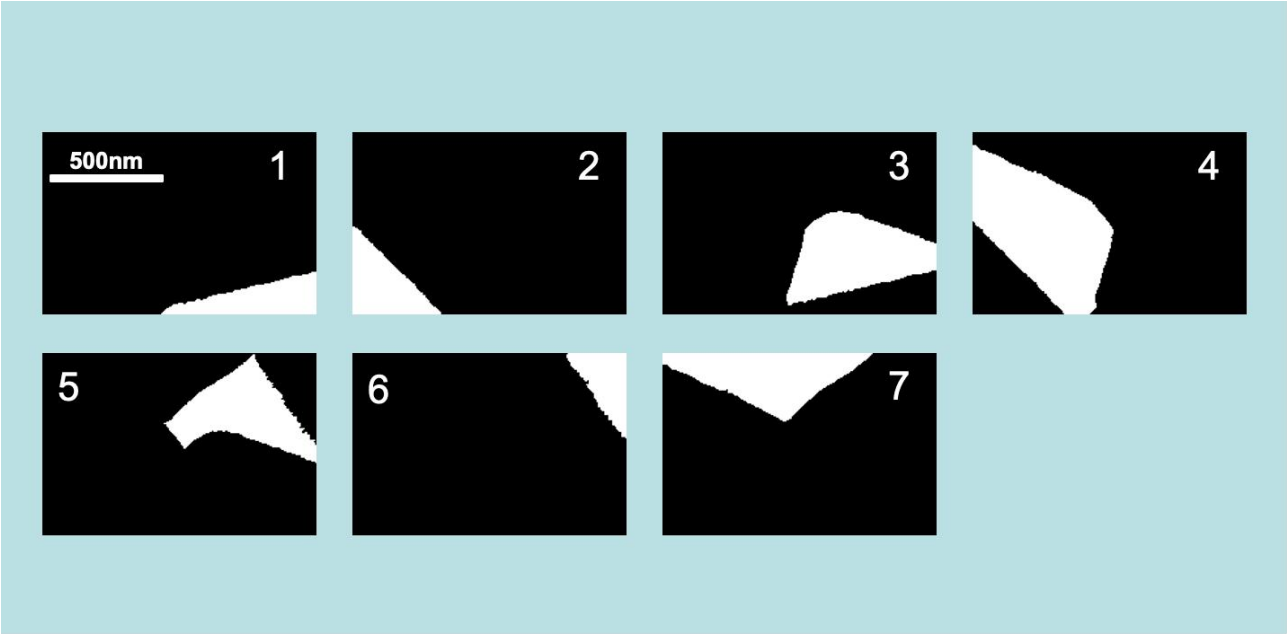

Fig. 3.6 Binary masks of major grains. White areas are grain interiors; black areas are background or boundaries.

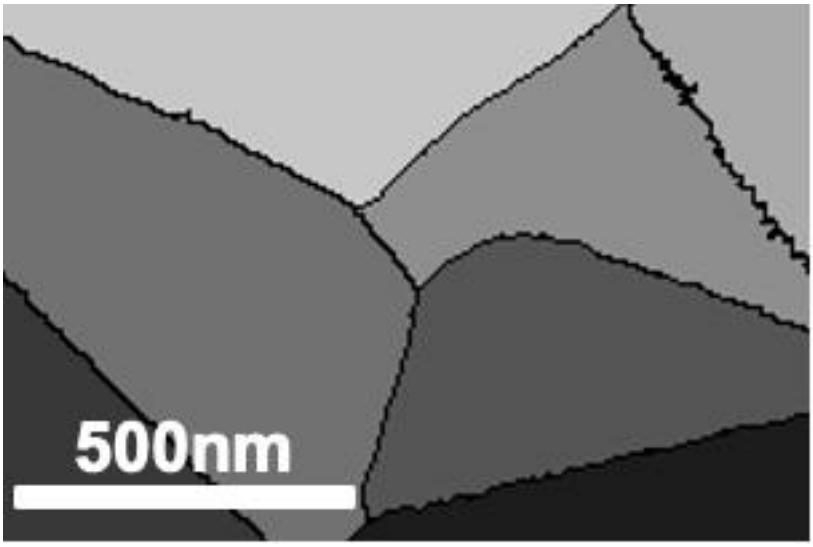

Fig. 3.7 Grain-label images. Different gray levels indicate different grains; black (0) marks background or boundaries.

3.3.2 Optimize

In this study, the grain boundary extraction algorithm introduces a method named Optimize (a custom algorithm developed in this work) when segmenting the grain interior and grain boundary regions. Optimize enables simultaneous consideration of an arbitrary number of basis images for linear-combination fitting during the computational process. Unlike previous approaches that treated W merely as the proportions contributed by two adjacent grains, this study extends the number of bases to three and explicitly defines $W= [w_A, w_B, w_C]$ as the vector of contribution coefficients from the three basis diffraction images. This improvement allows us to obtain an optimized W by minimizing the error between the combined basis and the actual diffraction pattern, thereby achieving higher accuracy in separating complex grain boundaries (e.g., triple-junction regions).

First, for each grain involved in the computation, all diffraction patterns within its region are extracted and averaged to obtain representative diffraction images. Fig. 3.8 shows the averaged diffraction image. This step utilizes the mask images of individual grains, reading all diffraction patterns corresponding to the white regions of the masks, and then averaging them to produce three average diffraction images, which are used as basis images.

Next, Fig. 3.9 illustrates the computation region definition, where the mask regions of adjacent grains and the interfacial grain-boundary pixel regions are combined. This ensures that the input

data include not only the transitional zone across the grain boundary but also representative information from the interiors of each grain.

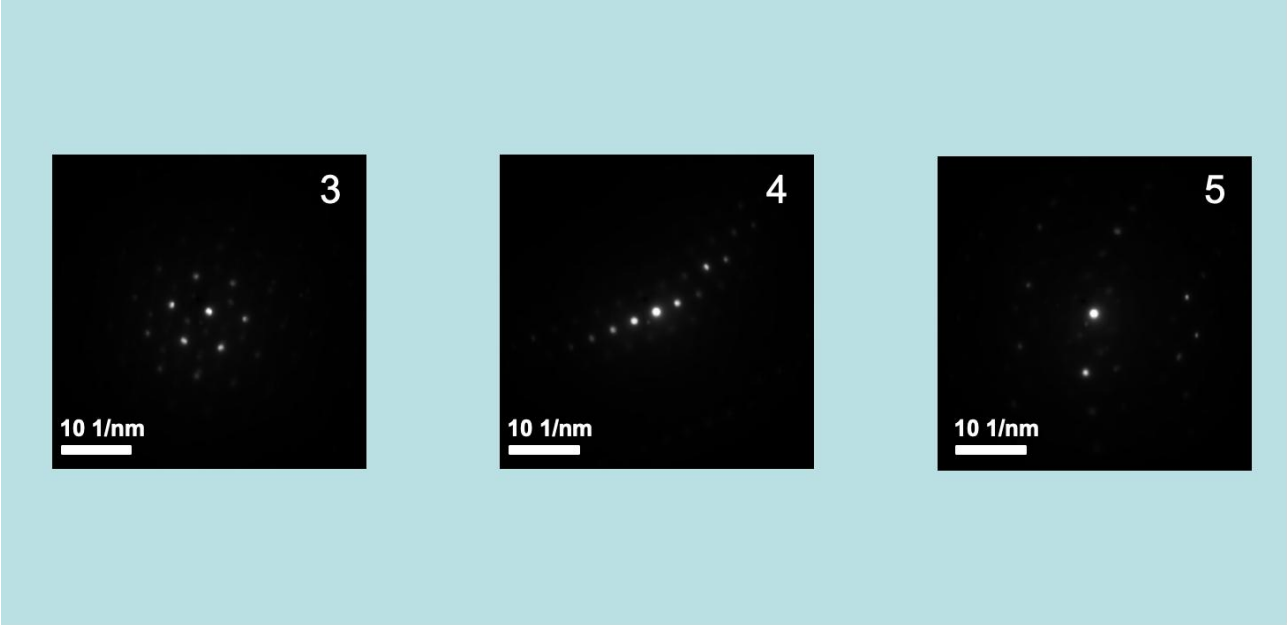

Fig. 3.8 Averaged diffraction images for selected grains.

Fig. 3.9 Definition of the computation region by combining adjacent grain interiors and boundary pixels.

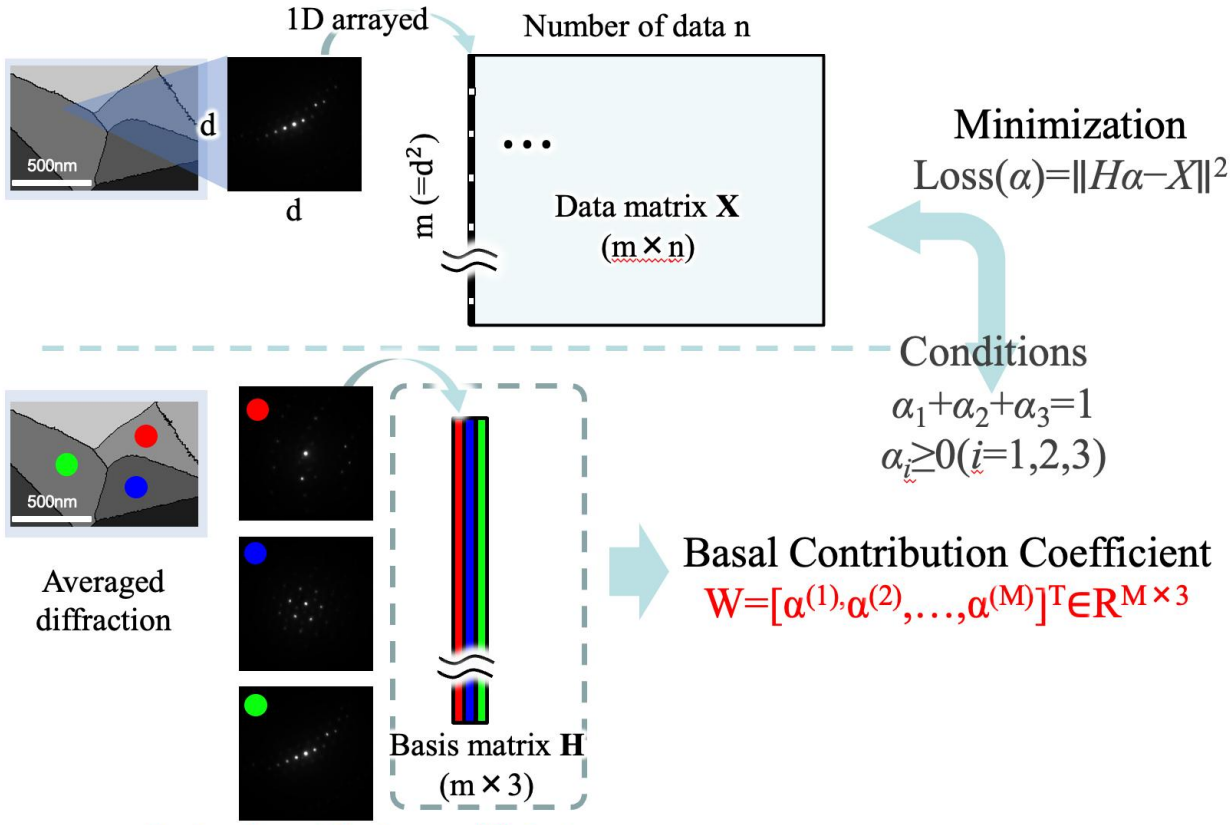

Fig. 3.10 Conceptual diagram of the Optimize calculation process.

Subsequently, according to the workflow shown in Fig. 3.10, all n diffraction patterns within the defined region (each pattern represented as an $d \times d$ matrix) are flattened into one-dimensional vectors of length m and stacked row-wise to form a data matrix X (with dimensions $m \times n$). Simultaneously, the three average diffraction images are combined to form the basis matrix H (with dimensions $m \times 3$). The optimization then solves for the coefficient matrix W by minimizing the squared error $\| HW - X \|^2$. To ensure physical interpretability, the following constraints are imposed on each column of coefficients:

$$\alpha_1 + \alpha_2 + \alpha_3 = 1, \quad \alpha_i \geq 0 \ (i = 1, 2, 3) \quad \#(3\text{-}1)$$

A custom script described in Section 2.11 is employed to perform the optimization for the diffraction vector at each pixel, iteratively updating $\alpha = \left[\alpha_1, \alpha_2, \alpha_3\right]^T$. The final output W, a coefficient matrix of size $m \times n$, assigns to each column (corresponding to a pixel) three weights

$\alpha_1, \alpha_2, \alpha_3$, which intuitively reflect the contribution of each grain to the diffraction pattern measured at that pixel location through a linear combination of the three basis images.

Through this three-basis Optimize fitting, not only is the ability to separate diffraction components of different grains in complex overlapping regions significantly enhanced, but the transitional features at grain boundaries also become clearer. Fig. 3.11 individually displays the resulting coefficient maps α_1 , α_2 , and α_3 side by side, clearly showing the spatial contribution from each grain. This provides a clear visual reference and lays a solid foundation for subsequent grain-boundary extraction and quantitative characterization.

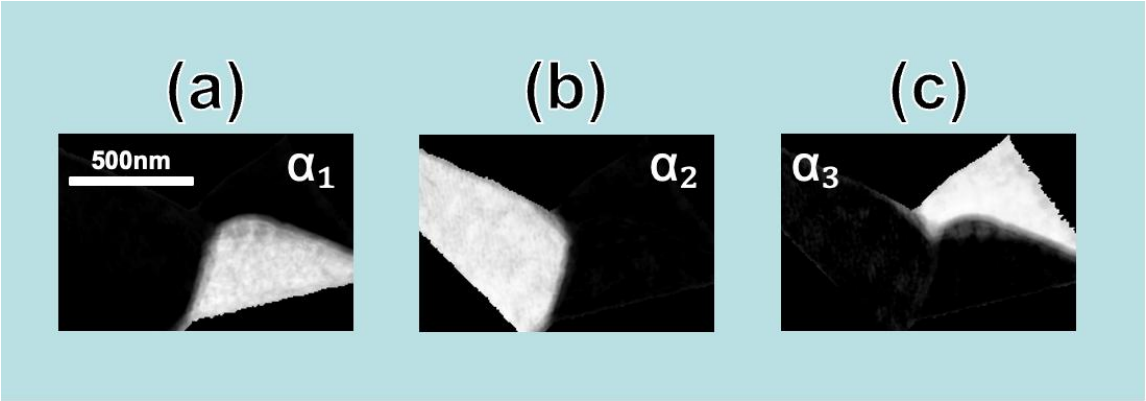

Fig. 3.11 Maps of the optimized contribution coefficients: (a) α_1 , (b) α_2 , and (c) α_3 .

3.3.3 Application of Optimize–Clustering in Grain Boundary Detection

For each pair of grain regions obtained from the previous segmentation step, this study introduces a spectral clustering method to automatically distinguish pixels belonging to grain interiors from those in the grain-boundary transition zones. Traditional ASTAR methods determine crystal orientations by template-by-template matching, whereas the method implemented in our program constructs a similarity graph from Optimize-output weight vectors and applies spectral clustering without using any predefined crystallographic template library. It directly utilizes differences in weight-vector distributions and groups regions with similar patterns through clustering analysis, thereby identifying the locations of grain boundaries. The basic concept is that weight vectors within a single grain should exhibit high similarity, while weight vectors across a grain boundary should differ significantly. Consequently, each scanned pixel is treated as a node in a graph, with the similarity of weight vectors defining the edge weights between nodes.

The similarity between nodes is typically defined using a Gaussian kernel:

$$W_{ij} = exp\left(- \frac{\| x_i - x_j \|^2}{2\sigma^2} \right) \quad \# (3\text{-}2)$$

where W_{ij} is the element of the similarity (weight) matrix W, x_i and x_j are the 3-dimensional weight vectors obtained after the Optimize step, defined as $x_i=[w_A(i), w_B(i), w_C(i)]$ for pixel i and $x_j=[w_A(j), w_B(j), w_C(j)]$ for pixel j. Each weight component (w_A, w_B, w_C) represents the fitted contribution of a specific basis diffraction pattern to the diffraction at that pixel. Here, σ is a scale parameter controlling neighborhood sensitivity. The set of all edges is denoted as E. From the weight matrix W, we construct the degree matrix D as a diagonal matrix with entries $D_{ii} = \sum_j W_{ij}$. To avoid confusion, the symbol D is reserved for the degree matrix, while distance measures (if any) are represented by δ.

Clustering can be formulated as an optimization problem. The goal is to partition the nodes of G into groups with strong internal connections and weak connections between groups. A widely used criterion for this is the normalized cut function:

$$Ncut(A,B) = \frac{cut(A,B)}{assoc(A,V)} + \frac{cut(A,B)}{assoc(B,V)} \quad \# (3\text{-}3)$$

where A and B are two disjoint subsets of nodes, cut(A,B) is the total weight of edges between A and B, and assoc(A,V) is the sum of weights from A to all nodes. Minimizing this objective function can be reformulated as an eigenvalue problem of the normalized graph Laplacian:

$$L_{sym} = D^{-\frac{1}{2}} (D - W) D^{-\frac{1}{2}} \quad \# (3\text{-}4)$$

A fundamental result in graph theory states that the multiplicity of the zero eigenvalue of L equals the number of connected components in the graph. Let k denote the desired number of clusters (or connected components in the ideal case). If the graph splits into k disconnected subgraphs, then L has exactly k zero eigenvalues, and their corresponding eigenvectors are indicator

vectors for those subgraphs. In practice, graphs are not perfectly disconnected, but if inter-cluster weights are much smaller than intra-cluster weights, then the smallest k eigenvalues will be close to zero, and their eigenvectors provide approximate indicators of cluster membership.

Collecting the first k eigenvectors of L yields an embedding matrix:

$$Y = \left[y_1, y_2, \ldots, y_k \right] \quad \# (3\text{-}5)$$

where each row of Y is a k-dimensional representation of a node. In this embedded space, nodes from the same cluster are located close to each other. k-means clustering is then applied to the rows of Y, and the resulting cluster labels are mapped back to the original nodes to complete clustering.

For regions containing only two grains, in principle k = 2 is sufficient to classify pixels into two categories corresponding to grain A and grain B. However, diffraction patterns of pixels in the transition zone near the boundary often exhibit mixed characteristics and dividing them into only two categories tends to misassign them to either side, thereby failing to identify the boundary as a separate entity. In this study, because the extraction is directly performed on a triple-junction region involving three grains, the initial k value is set to 4, where k denotes the pre-specified number of clusters: three clusters correspond to the three grain interiors, and one cluster represents the combined grain-boundary region. During experimentation, the results with k = 4 were not always optimal, so k was increased to 6, resulting in six clusters: three for the grain interiors and three for the individual grain boundaries. Although increasing k separates the three boundaries into distinct clusters rather than merging them, the complete set of grain boundaries can be obtained by simply combining these boundary-related clusters through pixel-wise addition.

For triple junction regions where three grains intersect, the three-basis Optimize fitting results described in Section 3.3.2 are directly used as input to this clustering process, so no separate algorithm is required.

3.4 Validation of Grain Boundary Extraction

First, a qualitative validation was performed. By comparing diffraction patterns on both sides of each detected boundary, we confirmed that within a single grain, diffraction signatures remain highly consistent, whereas across a boundary, the diffraction signatures change distinctly.

First, a qualitative validation was performed. By comparing diffraction patterns on both sides of each detected boundary, we confirmed that within a single grain, diffraction signatures remain highly consistent, whereas across a boundary, the diffraction signatures change distinctly.

In addition to these procedures, for quantitative validation, we further extracted cosine similarity between adjacent pixels along several predefined straight lines crossing grain boundaries. For each pair of neighboring pixels p_i and p_{i+1} on a line, the feature vectors at these positions are denoted as x_i and x_{i+1}, respectively. The cosine similarity is then defined as

$$\cos inesim\left(x_i, x_{i+1} \right) = \frac{x_i \cdot x_{i+1}}{\| x_i \| \ \| x_{i+1} \|} \quad \#(3\text{-}6)$$

Within a homogeneous grain, neighboring pixels exhibit highly similar diffraction features, leading to cosine similarity values consistently close to 1. When the sampling path enters a gray-band transition zone where diffraction patterns from adjacent grains are mixed, the similarity between neighboring pixels drops sharply. Once the path exits the gray band into the next grain, similarity returns to high values. This characteristic profile—high similarity → sudden drop → high similarity—directly indicates that the clustering method isolates transition zones and does not erroneously assign them to grain interiors, thus demonstrating the robustness and accuracy of boundary extraction.

In order to evaluate and compare the stability of extracted boundary widths, we performed a quantitative analysis based on distance transformation. For each binary grain-boundary map B(x,y), where x and y denote the horizontal and vertical pixel coordinates respectively, B(x,y)=1 represents a boundary pixel (foreground) and B(x,y)=0 represents a non-boundary pixel (background). A

Euclidean distance transform was applied to obtain the minimum distance from each boundary pixel (x,y) to the nearest background pixel (u,v):

$$D(x,y) = \min_{(u,v) \in Background} \sqrt{(x-u)^2 + (y-v)^2} \quad \#(3\text{-}7)$$

where D(x,y) is the local half-width at position (x,y). The full boundary width at that pixel is then calculated as:

$$W(x,y) = 2 \times D(x,y) \quad \#(3\text{-}8)$$

where W(x,y) represents the local width in pixels. The set of all sampled boundary pixels was traversed in raster order to form a width-variation sequence:

$$\{W_1, W_2, \ldots, W_N\} \quad \#(3\text{-}9)$$

where W_i is the measured local width at the i-th sampling point and N is the total number of sampling points. A width-variation curve is plotted with the horizontal axis representing the sampling index i along the boundary path and the vertical axis representing the corresponding local width W_i in pixels. Peaks in this curve indicate regions where the extracted boundary appears locally wider, while troughs indicate regions where the boundary appears narrower, reflecting local fluctuations in extraction stability. To quantify these fluctuations, the standard deviation of the width sequence is computed as:

$$\sigma = \sqrt{\frac{1}{N} \sum_{i=1}^{N} \left(W_i - \bar{W} \right)^2} \quad \#(3\text{-}10)$$

where the mean width $\bar{W}$ is:

$$\bar{W} = \frac{1}{N} \sum_{i=1}^{N} W_i \quad \#(3\text{-}11)$$

A smaller standard deviation σ indicates that the width along the boundary fluctuates less, which corresponds to more stable and consistent extraction.

Chapter 4 Results and Discussion

4.1 Segmentation of Grain Regions and Grain Boundaries in 2D TEM Diffraction Images

The proposed constrained optimization–based adaptive diffraction pattern decomposition–agglomerative clustering method was applied to two-dimensional transmission electron microscopy (TEM) diffraction image datasets to automatically segment grain interiors and extract grain boundaries. Prior to detailed analysis, we compare our segmentation results with those obtained via conventional bright-field imaging and ASTAR orientation mapping.

Figure 4.1 presents a typical region comparison: (a) the original bright-field micrograph; (b) an ASTAR orientation map of the selected rectangular region indicated in (a), with an added color bar showing the inverse pole figure values; (c) the segmentation result obtained by the Optimize + Clustering (OC) method within the same region, where black areas correspond to pixels outside the analyzed area; and (d) an overlay comparison showing grain boundaries (GB) extracted by the OC method in red and those by ASTAR in white, with scale bars included for all maps.

In the bright-field image Fig. 4.1 (a), grain boundaries appear as high-contrast lines; however, because the black boundary lines calculated by ASTAR are overlaid on the bright-field image, the original contrast at the boundaries is partially obscured. In addition, contrast is poor in certain areas due to variations in foil thickness, diffraction contrast, and noise—leading to spurious edges and weak boundary contrast that simple image-processing cannot reliably distinguish.

The ASTAR map Fig. 4.1 (b) colors each grain by orientation, so boundaries should lie at abrupt color changes; in the ASTAR system, a focused electron beam scans the specimen point by point, and at each pixel a convergent-beam or selected-area diffraction pattern is recorded. Each experimental diffraction pattern is then compared with a pre-computed template library using cross-correlation or similar matching algorithms, and the orientation corresponding to the highest match is assigned to that pixel. For this study on SUS316L austenitic stainless steel (face-centered cubic, fcc), the template library was generated from its crystallographic structure, calculating

simulated diffraction patterns for a wide range of orientations based on its lattice parameters. The resulting orientation information (e.g., Euler angles) is mapped to colors using an inverse pole figure scheme, producing the orientation map.

Because each pixel is assigned to the single orientation that best matches the templates, even when the electron beam transmits through overlapping grains, ASTAR depicts a boundary only where the dominant matched orientation changes—not directly due to mixed diffraction patterns. In practice, because many grain boundary surfaces are tilted rather than parallel to the electron beam, the projected boundary on the 2D map appears as a narrow line that is substantially thinner than the true boundary width. This limitation of ASTAR has already been illustrated in Fig. 1.3, which schematically shows how a tilted boundary surface results in such narrow boundary representations. The ASTAR map Fig. 4.1 (b) colors each grain by orientation, so boundaries should lie at abrupt color changes; however, because the electron beam may simultaneously sample adjacent grains, the resulting diffraction pattern is often a superposition of two grain patterns. This mixing causes orientation misassignment at boundary pixels—ASTAR thus renders boundaries as narrow black lines substantially thinner than the true boundary width.

In contrast, our method Fig. 4.1 (c) effectively separates pixel clusters belonging to different grains, rendering grain boundaries as continuous, irregular bands whose trajectories broadly match the actual boundaries observed in the bright-field image, even though the edges of these bands meander in a complex manner. In this analysis, the number of clusters was manually preset to $k = 4$ (corresponding to three grains and one boundary class), because $k = 4$ produced the best clustering performance among the tested values ($k = 4, 5, 6$), and this is the only parameter specified. Notably, no additional manual intervention or auxiliary image processing is required for our method to reveal grain boundaries in this way. This demonstrates that clustering based on diffraction-pattern differences can effectively discriminate interior grain pixels from transitional boundary pixels, enabling fully automatic boundary identification.

In Fig. 4.1(d), the grain boundaries extracted by the OC method are directly overlaid with those extracted by ASTAR, allowing a clear visual comparison of their trajectories and widths. The OC method delineates boundaries as continuous irregular bands that more closely follow the true

morphology observed in the bright-field image, whereas the ASTAR boundaries appear as narrower lines with occasional discontinuities. Notably, no additional manual intervention or auxiliary image processing is required for our method to reveal grain boundaries in this way. This demonstrates that clustering based on diffraction-pattern differences can effectively discriminate interior grain pixels from transitional boundary pixels, enabling fully automatic boundary identification.

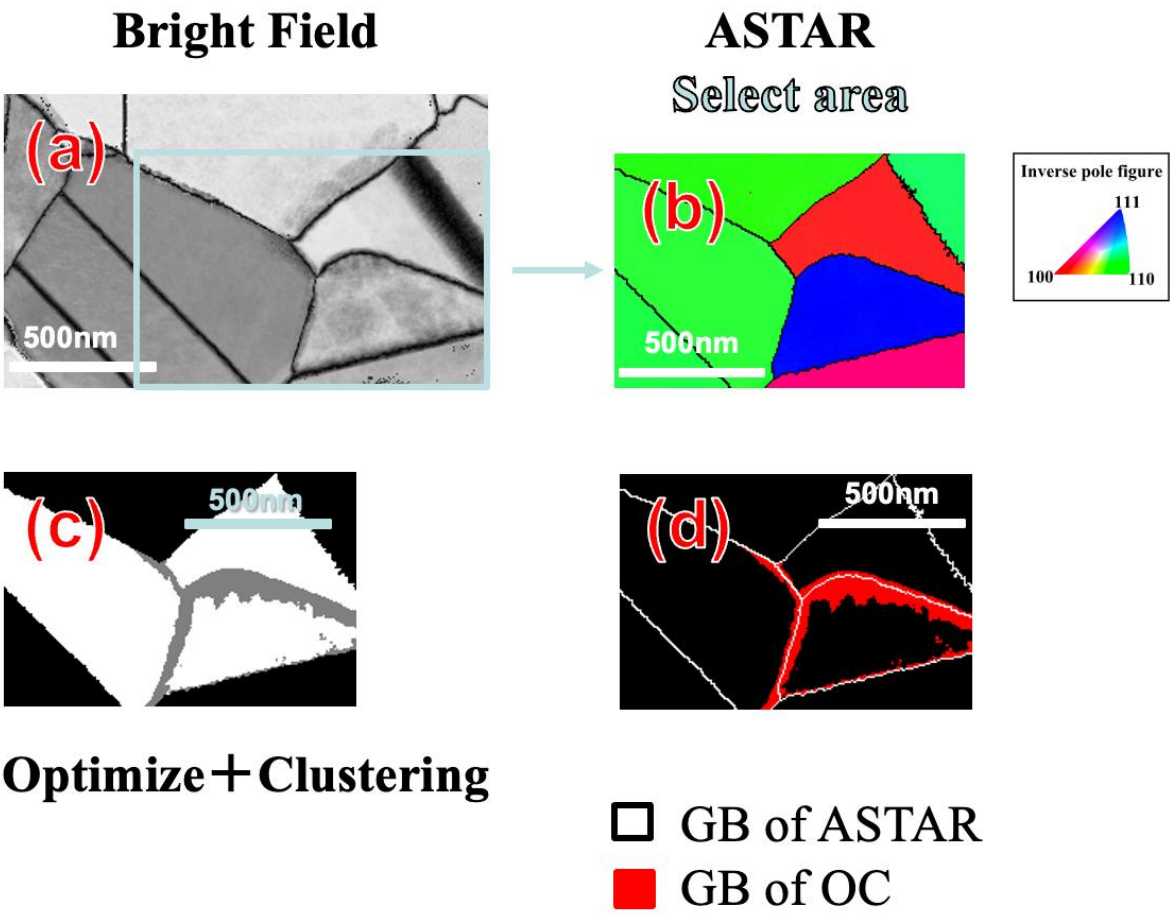

Fig. 4.1 Comparison of segmentation results in a representative region: (a) original bright-field image, with the analyzed area indicated by a rectangle; (b) ASTAR orientation map of the selected area with inverse pole figure color bar; (c) segmentation result obtained by the Optimize + Clustering (OC) method (black areas are outside the analyzed region); (d) comparison between grain boundaries extracted by the OC method (red) and those extracted by the ASTAR method (white).

4.2 Validation of the Superposition Principle for Boundary Diffraction Patterns

A key reason our method successfully detects grain boundaries is that the diffraction pattern in a boundary region can be regarded as a superposition of the patterns from the two adjacent grains. To validate this principle, we conducted targeted experimental observations. We selected one triple junction and its three emanating boundaries, then randomly chose five measurement points along each boundary. At each point, we first acquired a diffraction pattern at a tilt angle $\alpha = 0°$. Comparative analysis across boundary locations and tilt angles yielded the following observations.

As shown in Fig. 4.2 (a)-(b), diffraction patterns recorded on the boundary exhibit features from two distinct sets of diffraction spots. To validate the generated grain boundary, five mutually parallel sampling lines were randomly selected and drawn across the boundary region. Along each line, the red markers indicate pixels within grain 1 that are closest to the generated boundary, while the blue markers indicate pixels within grain 2 closest to the boundary on the opposite side. The green insets display diffraction patterns from three representative pixels along one sampling line: the pixel on the left side of the boundary region closest to grain 1, the pixel in the middle of the boundary region, and the pixel on the right side of the boundary region closest to grain 2.

When moving from either end toward the center of the boundary, the intensity of diffraction spots from the opposite grain gradually increases, culminating in a pattern at the center that contains spots from both grains simultaneously. These results strongly confirm that boundary-region diffraction patterns arise from the additive contributions of adjacent grain patterns. This experimentally underpins our decomposition–clustering approach: since mixed patterns occur at boundaries, we can employ a model comprising multiple substrate patterns to fit and separate the mixed signal into its constituent grain components, thereby pinpointing boundary locations.

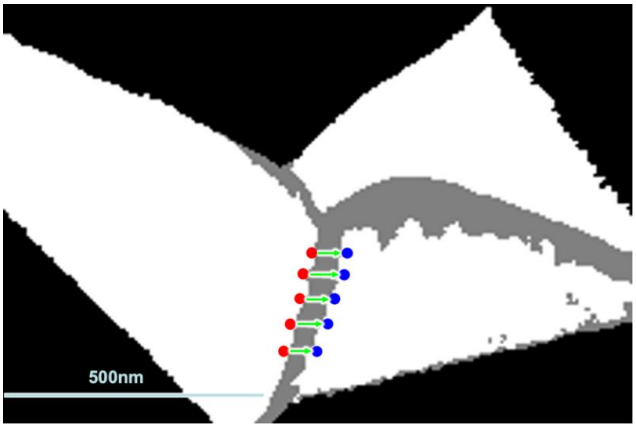

Fig. 4.2(a) Positions of the five sampling lines used for quantitative validation.

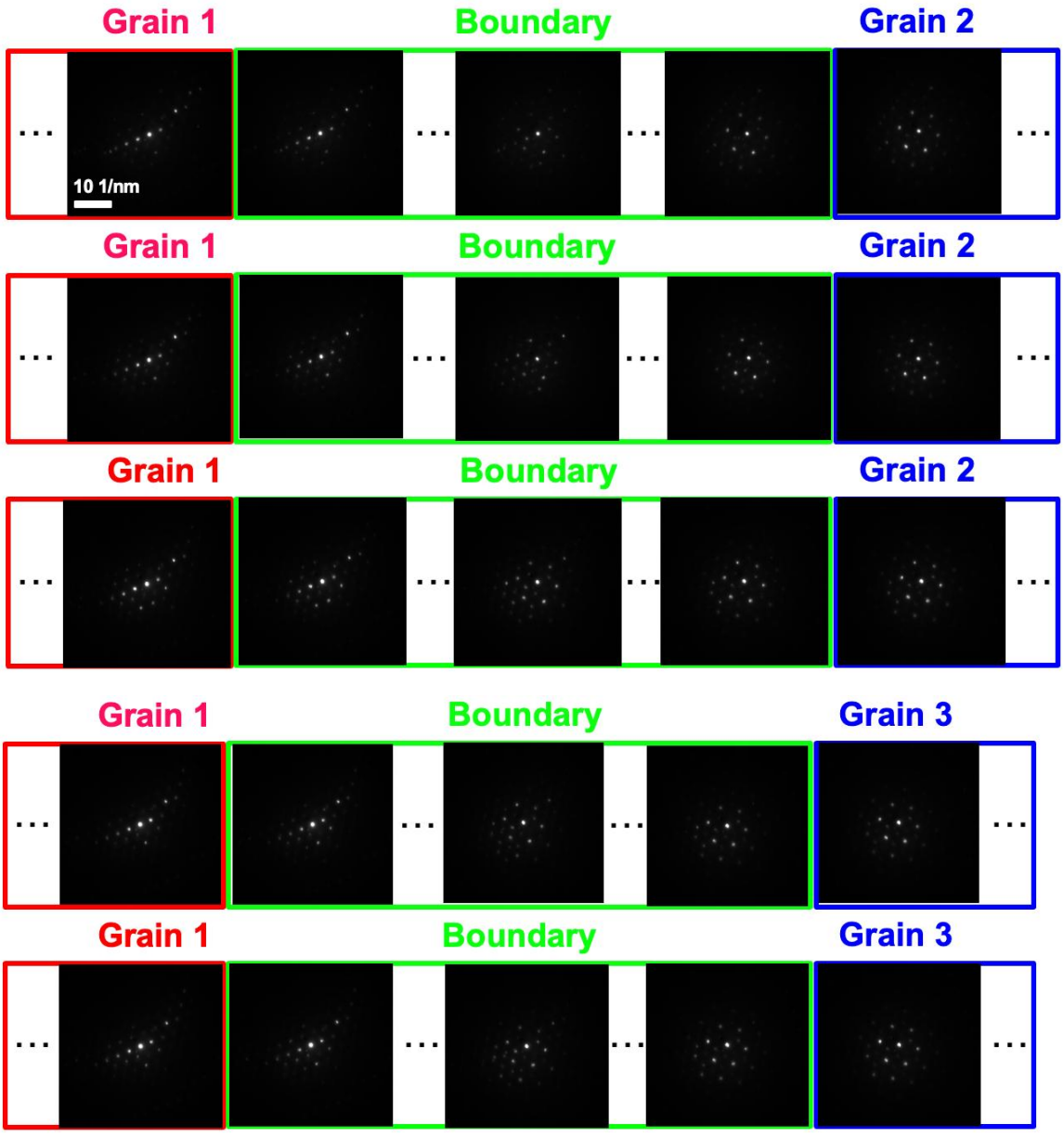

Fig. 4.2(b) Diffraction patterns acquired at the two ends and at the center of the grain boundary at a tilt angle of $\alpha = 0°$.

To provide a robust quantitative validation beyond qualitative inspection, we analyzed cosine similarity along five predefined sampling paths across the detected boundaries. For every adjacent pair of pixels along these lines, the feature vectors derived from the diffraction patterns were compared, and cosine similarity was calculated as described in Chapter 3.

In Fig. 4.3(a)–(e), the horizontal axis represents the step index along each sampling path, starting from one side of the boundary and moving pixel by pixel to the other side. The vertical axis represents the cosine similarity value computed between adjacent pixels at each step, with a value of 1.0 indicating identical diffraction features and lower values indicating greater differences. Each curve thus visualizes how the diffraction-feature similarity evolves across the path, and the smooth high-similarity segments at both ends of each curve correspond to grain interiors, while the sharp valley corresponds to the gray-band transition region.

As illustrated in the revised Fig. 4.3(a)–(e), black markers (labeled “OC”) denote the two boundary-edge positions determined by the proposed Optimize–Clustering method, while green markers (labeled “Sato”) show the edges detected by the Sato’s piecewise-regression method on the same region. This side-by-side indication enables a direct and fair comparison of the two approaches.

The resulting profiles, shown in Fig. 4.3, exhibit highly consistent behavior: In all five sampling lines, when traversing within a single grain, cosine similarity remains nearly constant at values very close to 1.0, confirming that diffraction patterns of neighboring pixels inside the same grain are almost identical. As the path approaches and crosses the boundary transition zone, cosine similarity shows a rapid and pronounced drop, reaching a clear minimum where the mixed diffraction patterns are dominant. Upon exiting the transition zone and entering the neighboring grain, cosine similarity quickly recovers to the high plateau, again approaching unity.

A noteworthy outcome of this comparison is that the OC method tends to localize the region of strongest diffraction-pattern transition within a narrower range, resulting in boundary edges that are overall tighter than those obtained by the piecewise-regression method. The piecewise-regression method extends the boundary outward to include regions where residual diffraction features from adjacent grains are still present, which is physically reasonable because diffraction mixing

continues in those areas. In contrast, the OC method tends to cut off part of this mixed zone earlier and therefore underestimates the absolute boundary width in certain locations, although it shows good continuity and handles complex junctions effectively. This indicates that, while the OC method can clearly detect clustering and transitions, there remains room for improvement in fully capturing the physical extent of grain-boundary regions.

Furthermore, by closely examining Fig. 4.3(e) together with Fig. 4.2(b) for grain 1, it is evident that in some local regions the edges of the OC-extracted boundary still lie within the true boundary zone (i.e., under-extraction). This indicates that although the OC method successfully isolates boundaries and handles triple junctions robustly, there remains a limitation in the absolute accuracy of the extracted boundary width.

These findings highlight both the strength and the current limitation of the OC method: while it provides a novel solution for handling complex triple-junction regions, it tends to underestimate boundary widths. This characteristic, clearly reflected in the similarity profiles, suggests that there is potential to improve the method by introducing additional constraints or refinement strategies.

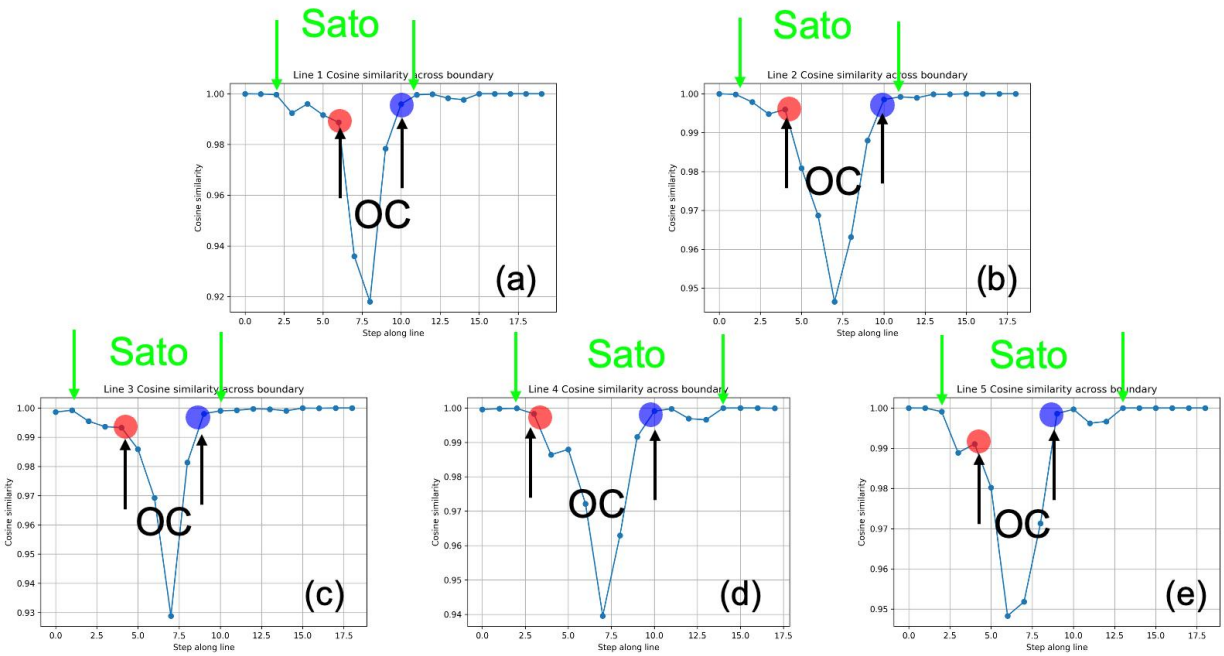

Fig. 4.3 (a)-(e) Cosine similarity profiles measured along five sampling lines crossing the grain boundary.

4.3 Quantitative Evaluation of Boundary Width Variation

To further verify the practical accuracy of the proposed method, a quantitative evaluation of local boundary width variation was carried out in direct comparison with Sato’ s piecewise-regression method’s fitting-based method. Two binary grain-boundary maps were prepared from the same field of view (see Fig. 4.1): one produced by the Optimize + Clustering (OC) method, and one generated by Sato’ s piecewise-regression method.

The motivation for developing the new method originated from the observation that Sato’ s piecewise-regression method was difficult to apply directly to the type of samples used in this study. In order to enable Sato’s piecewise-regression method to produce a valid output for comparison, a smaller region than that chosen in Fig. 4.2 was selected for this test—while still containing three grain boundaries. This selection ensures that piecewise-regression method can function properly on this subset while maintaining representative features of the boundary network.

For each binary boundary image, a distance-transform algorithm was applied to compute the local half-width at every white-pixel location. The full boundary width at each pixel was then estimated as twice the distance to the nearest black pixel. To ensure fair comparison, 500 sampling points were extracted along the main grain boundaries. The sequence of local widths along the boundary was plotted as a curve, and the standard deviation of these width values was calculated as a measure of stability. A smaller standard deviation indicates that the method produces a more consistent boundary width along the grain boundary, which in turn reflects better measurement precision.

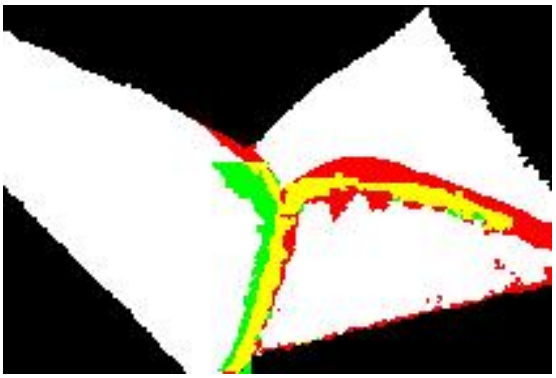

Fig. 4.4 Comparison of width-variation curves along the grain boundary for the OC method (red) and Sato’s method (green).

Fig. 4.4 shows the resulting width-variation curves for both methods. The OC method (red) exhibits a mean width comparable to Sato's piecewise-regression method (green, and the yellow regions indicate where the two methods overlap), and both methods show fluctuations along the main boundary segments. While minor variations appear near complex junctions, the OC method's curve maintains a trend that is overall comparable to that of Sato's piecewise-regression method. Based on the verification using diffraction patterns on both sides of the boundaries in Fig. 4.2, the boundaries extracted by the OC method are confirmed to be more accurate; therefore, the large green region given by Sato's piecewise-regression method does not correspond to an actual grain boundary for this sample.

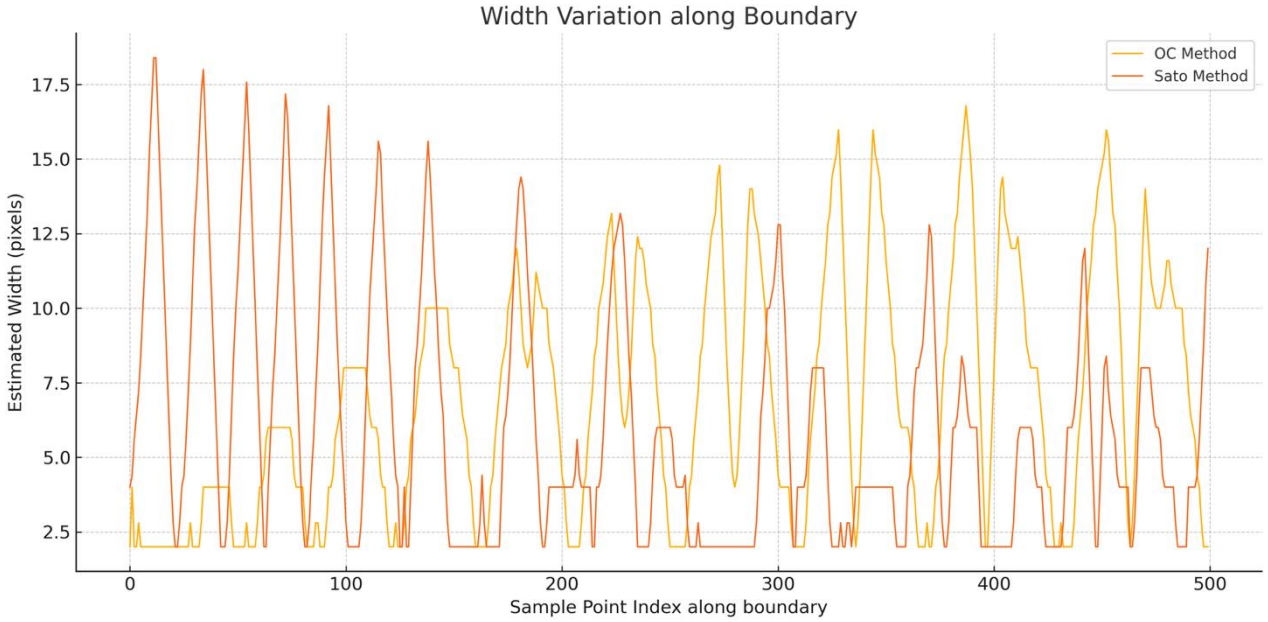

Fig. 4.5 Box plot of width distributions for both methods.

Fig. 4.5 shows the width-variation curves for both methods. The horizontal axis represents the sampling index along the extracted boundary, that is, the order of measurement points following the path of the boundary. The vertical axis represents the estimated local boundary width in pixels. Peaks in the curve indicate positions where the boundary appears locally wider, while troughs correspond to positions where the boundary appears narrower. According to the evaluation criterion described earlier—that smaller variation in width along the boundary indicates higher measurement stability—these peaks and troughs visualize the local fluctuations of each method. Both methods

exhibit fluctuations along the boundary, but a method with fewer or less pronounced peaks and troughs is considered to provide a more consistent extraction.

The OC method (red) and Sato's piecewise-regression method (green, with yellow indicating overlap between the two methods) show similar mean widths, yet the OC method demonstrates a slightly more stable trend, reflected in its standard deviation of 4.00 pixels compared to 4.07 pixels for piecewise-regression method. This further supports that, for this sample, the OC method yields more consistent and reliable boundary width measurements.

These results clearly indicate that the OC method yields a slightly more stable boundary width measurement compared with Sato's method. Even though the numerical difference in standard deviation is modest, the improvement demonstrates that the clustering-based approach not only avoids the need for prior template information but also provides superior local width consistency. The comparison validates that our method achieves pixel-level localization with reduced width fluctuations, confirming its robustness. This advantage highlights the OC method as a practical and reliable alternative, with further potential for refinement—such as integrating local slope constraints or adaptive smoothing—to deliver even greater precision in future work.

4.4 Advantages of the Diffraction-Pattern Decomposition–Clustering Method in Boundary Continuity and Localization Precision

The comparisons and validations above demonstrate significant advantages of our method in grain-boundary detection. First, in terms of localization precision, our method yields boundary positions that closely follow the true boundaries, whereas the ASTAR method itself is not designed to output the actual physical grain boundary.

Second, regarding boundary continuity, our method correctly identifies mixed-pattern pixels and distinguishes them from grain-interior pixels, resulting in continuous, unbroken boundary lines rather than fragmented segments. This continuity is crucial for downstream analyses (e.g., three-dimensional reconstruction of boundaries), as continuous boundaries more accurately represent grain shape and size.

Third, our method offers superior applicability and automation. Traditional improved approaches—such as combining ASTAR with Optimize fitting—require first identifying candidate boundary regions via ASTAR, then assuming that boundary-pixel patterns are linear combinations of two grain patterns and iteratively fitting to determine the mixing ratio for each pixel. A segmented linear-regression step along the boundary direction is then needed to locate abrupt changes in mixing ratios and thereby determine boundary endpoints. Although this can enhance boundary resolution, it involves complex workflows and requires prior knowledge of the number of grains involved (i.e., the number of substrate patterns). In contrast, our clustering method is entirely orientation-index–free: it accepts all pixel diffraction patterns as input, automatically classifies them into clusters—each corresponding to a grain—and naturally delineates boundaries where cluster membership changes. No reference patterns are needed a priori; the algorithm autonomously identifies classification boundaries based on pattern differences.

Consequently, even when diffraction patterns are blurred by dislocation strain or other factors making indexing difficult, the clustering method reliably locates boundaries. Moreover, because it processes the entire field of view in one pass—rather than matching each pixel as in ASTAR or fitting each boundary segment as in MLS—it is also more efficient. Finally, in complex scenarios

such as junctions involving four or more grains, the clustering method inherently partitions the region into the appropriate number of clusters, enabling simultaneous detection of multiple boundaries without separate treatment for each grain pair.

Overall, the results and discussion presented in this chapter demonstrate that the diffraction-pattern decomposition–clustering approach outperforms conventional bright-field and ASTAR analysis in reliability, accuracy, and applicability, offering a powerful new avenue for grain-boundary analysis and laying a robust foundation for further boundary characterization and extended studies.

Chapter 5 Summary and Outlook

5.1 Summary of This Study

This study developed a novel method for automatic grain-boundary detection based on diffraction-pattern decomposition and Optimize–Clustering analysis, aiming to improve accuracy and efficiency. First, we reviewed the importance of three-dimensional grain-boundary characterization and identified the limitations of current techniques in terms of precision and practicality, noting that traditional ASTAR template-matching suffers from imprecise boundary localization, dependence on prior template libraries, and difficulty handling multi-grain junctions. To address these issues, we proposed the "constrained-optimization diffraction-pattern decomposition–Optimize–Clustering" algorithm. This method utilizes 4D-STEM diffraction data directly—without requiring a prebuilt template library—and clusters pixels based on Optimize-output weight-vector differences to identify grain boundaries. Its core innovation is the application of Optimize–Clustering for unsupervised classification of all scan-area pixels, automatically distinguishing grain interiors from boundary transition zones. For complex regions such as triple junctions, we introduced a constrained-optimization strategy for multi-basis linear decomposition to separate overlapping diffraction signals from multiple grains in a single step, avoiding the cumbersome pairwise fitting required by conventional approaches.

Experimental validation yielded the following key conclusions: First, in two-dimensional projections, the proposed method extracts boundary positions with pixel-level precision, substantially improving upon the localization errors and discontinuities present in ASTAR orientation maps. Notably, for complex boundary networks (e.g., triple junctions), our method requires no manual intervention and successfully identifies all intersecting boundaries in a unified procedure, overcoming the prerequisite of knowing all grain pairs and fitting them separately in ASTAR + MLS. Second, compared with template-matching ASTAR, our approach eliminates reliance on prior template libraries, thus avoiding matching errors arising from unknown crystal structures or lattice distortions. Even in regions where pattern indexing fails due to orientation gradients or dislocation strain, Optimize–Clustering based on weight-vector differences reliably localizes boundaries, enhancing universality and robustness. Third, in computational efficiency, Optimize–Clustering processes the entire field of view in one pass—more efficient than ASTAR's per-pixel matching and MLS's per-boundary fitting. As data volume grows, matrix-decomposition clustering benefits from linear-algebra optimizations, whereas template-matching time scales linearly with library size. Overall, the proposed method offers significant improvements in accuracy, completeness, and automation over conventional techniques, laying a solid foundation for further boundary-characterization research.

5.2 Future Work

Despite the promising results, there remain avenues for refinement and extension. First, applying this method to materials with more complex microstructures—such as heavily textured deformed metals, subgrain structures with continuous orientation gradients, or specimens containing mechanical twins—could test its adaptability. In such cases, boundaries may be highly tortuous or involve four or more grains. Although the Optimize–Clustering framework can, in principle, accommodate multiple clusters by increasing k, parameter selection and numerical stability for extreme topologies will require further investigation. Introducing adaptive parameter tuning—such as automatically determining k from the eigenvalue spectrum—may enhance effectiveness across varied morphologies.

Second, combining diffraction-pattern decomposition–Optimize–Clustering with other microscopy modalities could enrich boundary detection. For example, integrating bright-field or annular-dark-field images with diffraction data through multimodal analysis may improve detection of low-contrast boundaries. Correlating TEM results with EBSD maps would enable cross-validation and calibration at larger scales. In chemically complex systems, fusing EDS/EELS elemental maps could aid in distinguishing phase boundaries. Multimodal data fusion would extend boundary detection beyond single-criterion approaches, enhancing discrimination under complex backgrounds.

Third, this work focuses on two-dimensional boundary extraction and validation. A next goal is three-dimensional reconstruction and visualization of grain boundaries by combining boundary projections from multiple tilt angles. For instance, matching boundary pixels between alpha=0° and alpha=20° datasets via stereoscopic correspondence could compute spatial depth and reconstruct boundary trajectories in three-dimensional space. With additional tilt datasets, algorithms analogous to electron tomography could yield full 3D boundary volumes. Such reconstructions would enable quantitative analysis of boundary curvature, connectivity, and true topography—critical for understanding boundary effects on material behavior. Furthermore, applying this method to in situ experiments could enable continuous tracking of boundary migration by stitching successive 3D reconstructions into dynamic evolution movies, revealing nanoscale migration and morphological changes. This capability would provide valuable insights for grain-boundary engineering and performance optimization.

In summary, the constrained-optimization diffraction-pattern decomposition–Optimize–Clustering method offers a viable new route for precise characterization of internal grain-boundary networks. Its advantages over traditional approaches—no template library, multi-boundary handling, high automation—position it for further enhancement through integration with computational imaging and machine-learning advances. Future development will extend its applicability to complex materials and three-dimensional boundary studies, enabling high-throughput, intelligent analysis of grain boundaries across diverse material systems and advancing microstructural design for optimized properties.

References

[1] Schuh C A, Kumar M, King W E. Analysis of grain boundary networks and their evolution during grain boundary engineering[J]. Acta Materialia, 2003, 51(3): 687-700.

[2] Kobler A, Kübel C. Towards 3D crystal orientation reconstruction using automated crystal orientation mapping transmission electron microscopy (ACOM-TEM)[J]. Beilstein Journal of Nanotechnology, 2018, 9(1): 602-607.

[3] Rauch E F, Véron M, Portillo J, et al. Automatic crystal orientation and phase mapping in TEM by precession diffraction[J]. Microscopy and Analysis-UK, 2008, 128: S5-S8.

[4] Li G, Zhang H, Han Y. 4D-STEM ptychography for electron-beam-sensitive materials[J]. ACS Central Science, 2022, 8(12): 1579-1588.

[5] ASTAR (EBSD-TEM like) Automatic Crystal Orientation/Phase mapping for TEM https://nanocrystallography.research.pdx.edu/wp-content/uploads/2020/07/BerlinASTARII.pdf

[6]佐藤俊介. 電子回折図形を基にした結晶粒界抽出およびその3次元可視化[D]. 九州大学, 2024.

[7] Rauch E F, Harrison P, Zhou X, et al. New features in crystal orientation and phase mapping for transmission electron microscopy[J]. Symmetry, 2021, 13(09): 1675.

[8] Rauch E F, Véron M. Automated crystal orientation and phase mapping in TEM[J]. Materials Characterization, 2014, 98: 1-9.

[9] Viladot D, Véron M, Gemmi M, et al. Orientation and phase mapping in the transmission electron microscope using precession-assisted diffraction spot recognition: state-of-the-art results[J]. Journal of microscopy, 2013, 252(1): 23-34.

[10] Shi Q, Zhou Y, Zhong H, et al. Indexation of electron diffraction patterns at grain boundaries[J]. Materials Characterization, 2021, 182: 111553.

[11] Tsivoulas D, Da Fonseca J Q, Tuffs M, et al. Measurement and modelling of textures in flow formed Cr-Mo-V steel tubes[J]. Materials Science and Engineering: A, 2017, 685: 7-18.

[12] Maurice C, Driver J H, Fortunier R. On solving the orientation gradient dependency of high angular resolution EBSD[J]. Ultramicroscopy, 2012, 113: 171-181.

[13] Doddapaneni S, Kumar S, Sharma S, et al. Advancements in EBSD Techniques: A Comprehensive Review on Characterization of Composites and Metals, Sample Preparation, and Operational Parameters[J]. Journal of Composites Science, 2025, 9(3): 132.

[14] Nzogang B C, Thilliez S, Mussi A, et al. Application of scanning precession electron diffraction in the transmission electron microscope to the characterization of deformation in wadsleyite and ringwoodite[J]. Minerals, 2018, 8(4): 153.

[15] Rauch E F, Harrison P, Zhou X, et al. New features in crystal orientation and phase mapping for transmission electron microscopy[J]. Symmetry, 2021, 13(09): 1675.

[16] Mariano R G, Yau A, McKeown J T, et al. Comparing scanning electron microscope and transmission electron microscope grain mapping techniques applied to well-defined and highly irregular nanoparticles[J]. ACS omega, 2020, 5(6): 2791-2799.

[17] Wei S, Zhang L, Zheng S, et al. Deformation-induced interfacial transition zone in Cu/V nanolamellar multilayers[J]. Scripta Materialia, 2019, 159: 104-108.

[18] Feng B, Lugg N R, Kumamoto A, et al. On the quantitativeness of grain boundary chemistry using STEM EDS: A ZrO2 Σ9 model grain boundary case study[J]. Ultramicroscopy, 2018, 193: 33-38.

[19] Khajehvand M. Crystal Misorietation and Defect Generation during Contact between Two Aluminum Substrates[J]. 2018.

[20] Johnson C L, Hÿtch M J, Buseck P R. Nanoscale waviness of low-angle grain boundaries[J]. Proceedings of the National Academy of Sciences, 2004, 101(52): 17936-17939.

[21] Li Y, Bushby A J, Dunstan D J. The Hall–Petch effect as a manifestation of the general size effect[J]. Proceedings of the Royal Society A: Mathematical, Physical and Engineering Sciences, 2016, 472(2190): 20150890.

[22] Zhao H, Xie J, Mao A, et al. Effects of heating mode and temperature on the microstructures, electrical and optical properties of molybdenum thin Films[J]. Materials, 2018, 11(9): 1634.

[23] Wolf D. Grain boundaries in nanocrystalline materials[M]//Handbook of Materials Modeling: Methods. Dordrecht: Springer Netherlands, 2005: 2055-2079.

[24] Johnson C L, Hÿtch M J, Buseck P R. Nanoscale waviness of low-angle grain boundaries[J]. Proceedings of the National Academy of Sciences, 2004, 101(52): 17936-17939.

[25] Midgley P A, Dunin-Borkowski R E. Electron tomography and holography in materials science[J]. Nature materials, 2009, 8(4): 271-280.

[26] Barron A R. Physical methods in chemistry and nano science[J]. 2015.

[27] Williams D B, Carter C B, Williams D B, et al. The transmission electron microscope[M]. Springer Us, 2009.

[28] Hayat M A E. Basic techniques for transmission electron microscopy[M]. Elsevier, 2012.

[29] Cowley J M, Moodie A F. The scattering of electrons by atoms and crystals. I. A new theoretical approach[J]. Acta Crystallographica, 1957, 10(10): 609-619.

[30] Ophus C. Four-dimensional scanning transmission electron microscopy (4D-STEM): From scanning nanodiffraction to ptychography and beyond[J]. Microscopy and Microanalysis, 2019, 25(3): 563-582.

[31] Seyring M, Simon A, Voigt I, et al. Quantitative crystallographic analysis of individual carbon nanofibers using high resolution transmission electron microscopy and electron diffraction[J]. Carbon, 2017, 116: 347-355.

[32] Hirata A. Local structure analysis of amorphous materials by angstrom-beam electron diffraction[J]. Microscopy, 2021, 70(2): 171-177.

[33] Rauch E F, Harrison P, Zhou X, et al. New features in crystal orientation and phase mapping for transmission electron microscopy[J]. Symmetry, 2021, 13(09): 1675.

[34] Differential Phase Contrast
https://www.gatan.com/differential-phase-contrast

[35] Wu M, Harreiß C, Ophus C, et al. Seeing structural evolution of organic molecular nano-crystallites using 4D scanning confocal electron diffraction (4D-SCED)[J]. Nature Communications, 2022, 13(1): 2911.

[36] Ophus C. Quantitative scanning transmission electron microscopy for materials science: imaging, diffraction, spectroscopy, and tomography[J]. Annual Review of Materials Research, 2023, 53(1): 105-141.

[37]Jeong J, Cautaerts N, Dehm G, et al. Automated crystal orientation mapping by precession electron diffraction-assisted four-dimensional scanning transmission electron microscopy using a scintillator-based CMOS detector[J]. Microscopy and Microanalysis, 2021, 27(5): 1102-1112.

[38] Rauch E F, Harrison P, Zhou X, et al. New features in crystal orientation and phase mapping for transmission electron microscopy[J]. Symmetry, 2021, 13(09): 1675.

Acknowledgements

My two years as a master's student have passed in the blink of an eye. The successful completion of this research would not have been possible without the generous support and guidance of many people. I would like to express my heartfelt gratitude to Professor Mitsuhiro Murayama, Associate Professor Hikaru Saito, and Assistant Professor Shiro Ihara of the Institute for Materials Chemistry and Engineering, Kyushu University.

First and foremost, I am deeply indebted to Assistant Professor Shiro Ihara for his meticulous guidance, warm encouragement, and patient instruction throughout these two years. Despite a demanding schedule, Assistant Professor Ihara personally taught me the operation of the transmission electron microscope and frequently reminded me to approach each experiment with diligence, responsibility, and an organized attitude. His consistent encouragement to identify, analyze, and solve problems independently has not only enhanced my professional knowledge but also honed my practical skills and problem-solving abilities. Beyond academic matters, Assistant Professor Ihara often offered valuable personal advice and sincere support during difficult times, for which I extend my highest respect and heartfelt thanks.

I am also sincerely grateful to Associate Professor Hikaru Saito, whose invaluable guidance and assistance in academic writing helped shape the quality of this thesis. His insightful comments and suggestions greatly improved my drafts, and the detailed feedback given during weekly group meetings—together with discussions among group members—broadened my knowledge and perspectives, making my master's studies truly fulfilling and meaningful.

Furthermore, my deepest appreciation goes to Professor Mitsuhiro Murayama for his careful guidance on my chosen research topic and for his strong encouragement throughout my studies. His advice and support have been of immeasurable value, and I am truly thankful.

Finally, I would like to express my heartfelt gratitude to my parents, as well as to my relatives and friends, for their constant care, support, and encouragement. I am also deeply appreciative of the professors and experts who, despite their busy schedules, took the time to review my thesis and participate in my defense.

July 2025

Xiaoge Liu